Article

A bioinspired Au-Cu$_{1.97}$S/Cu$_2$S film with efficient low-angle-dependent and thermal-assisted photodetection properties

Junlong Tian, Ruyi Qiao, Kai Xiong, Wang Zhang, Lulu Chen

jltian666@xtu.edu.cn (J.T.)
wangzhang@sjtu.edu.cn (W.Z.)

HIGHLIGHTS
Inspired by geological process, solid solution-atom enhancement in photoresponse

A photothermal-assist-enhanced and temperature-autoregulated photodetector

The photodetector exhibited excellent low-angle-dependent photodetection

Article

A bioinspired Au-Cu$_{1.97}$S/Cu$_2$S film with efficient low-angle-dependent and thermal-assisted photodetection properties

Junlong Tian,[1,4,5,*] Ruyi Qiao,[1,4] Kai Xiong,[2] Wang Zhang,[3,*] and Lulu Chen[1]

SUMMARY

Inspired by the geological processes, this study develops an innovative low-concentration-ratio H$_2$ reduction method to reduce the stoichiometric Au-CuS nanoparticles to produce completely reduced stoichiometric Cu$_2$S with "invisible" Au achieved for solid solution Au enhancement. A stable Au-Cu$_{1.97}$S/Cu$_2$S micro/nano-composite is then formed by spontaneous oxidation. From this composite, in combination with biomimetic technology, an omnidirectional photoabsorption and thermoregulated film (Au-Cu$_{1.97}$S/Cu$_2$S-C-T_FW) is designed and fabricated as a photothermal-assisted and temperature-autoregulated photodetector for broadband and low-angle-dependent photodetection that presents good performance with high responsivity (26.37 mA/W), detectivity (1.25×10^8 Jones), and good stability at low bias (0.5 V). Solid solution Au exhibits significantly enhanced photodetection (1,000 times). This study offers a new concept for improving the stability and photoelectric properties of copper chalcogenides. Moreover, it opens up a new avenue toward enhancing the performance of optoelectronic and photovoltaic devices using solid solution metal atoms and thermal-assisted, anti-overheating temperature autoregulation.

INTRODUCTION

Copper chalcogenide nanomaterials (Cu$_x$E with E = S, Se, or Te and x from 1 to 2) are regarded as a promising material for potential applications in energy resource (Wong et al., 2015; Jiang et al., 2015; Wu et al., 2008, 2019; Tian et al., 2015a; Joo et al., 2019; Zhuang et al., 2016; Yu et al., 2018), environmental (Manzi et al., 2015; Cui et al., 2015, 2016; Saranya et al., 2015) and medical therapy (Deng et al., 2017; Gao et al., 2018; Chang et al., 2018), and electron fields (Kriegel et al., 2012; Riha et al., 2011; Johari and Shenoy, 2011) that have drawn increasing attention due to their important semiconductor characteristics, with band gap energies of 1.0–1.5 eV (Wang et al., 2015) and plasmonic features (Luther et al., 2011) as well as tunable optical (Luther et al., 2011; Comin and Manna, 2014; Scotognella et al., 2011) and electronic properties (Riha et al., 2011). In particular, with its merits of being abundant, nontoxic, environment-friendly, and recyclable and having appropriate band gaps of ~1.2 eV (Kriegel et al., 2012), Cu$_2$S nanomaterials and their derived copper-deficient compounds have attracted a great deal of attention and have been highlighted as potential electronic (Riha et al., 2011; Liu et al., 2015), optoelectronic (Wong et al., 2015; Wu et al., 2008; Pan et al., 2012), photothermal (Wu et al., 2019; Tian et al., 2011, 2015a; Deng et al., 2017; Chang et al., 2018), photoelectrochemical (Yu et al., 2018; Han et al., 2016), and biosensor (Jia et al., 2019) materials. Unfortunately, except for the aforementioned merits, there are several hurdles to using Cu$_2$S nanomaterials that would extensively hinder their performance in electronic and photoelectronic applications. A significant limitation is that the highly reactive surface sites of Cu$_2$S nanomaterials are often prone to oxidation and are thermodynamically unstable when exposed to oxygen, because the surfaces of Cu$_2$S nanomaterials have large numbers of unpassivated surface sites (Kriegel et al., 2012; Riha et al., 2011). Recently, to address these stability issues, protective layers (such as the Al$_2$O$_3$ protective layer [Martinson et al., 2013] and CdS protective layer [Wong et al., 2015]) were deposited on the surface of Cu$_2$S, leading to progress in the stabilization of Cu$_2$S and implying future uses for Cu$_2$S nanomaterials in more efficient and stable electronic and photoelectronic devices. However, there exists a mismatch between the protective layer and the Cu$_2$S nanomaterials (Wong et al., 2015). Furthermore, the deficiencies in the copper vacancies are responsible for low free carrier (holes) concentrations in Cu$_2$S, which results in Cu$_2$S that exhibits relatively low conductivity and suppressed localized surface plasmons (LSPs) (Kriegel et al., 2012; Riha et al., 2011; Luther et al.,

[1]Hunan Key Laboratory of Micro-Nano Energy Materials and Devices, Laboratory for Quantum Engineering and Micro-Nano Energy Technology, School of Physics and Optoelectronic, Xiangtan University, Xiangtan, Hunan 411105, China

[2]College of Materials Science and Engineering, Yunnan University, Kunming, Yunnan 650091, China

[3]State Key Laboratory of Metal Matrix Composites, Shanghai Jiao Tong University, Shanghai 200240, China

[4]These authors contributed equally

[5]Lead contact

*Correspondence:
jltian666@xtu.edu.cn (J.T.),
wangzhang@sjtu.edu.cn (W.Z.)

https://doi.org/10.1016/j.isci.2021.102167

2011). Currently, numerous efforts have been devoted to circumventing these hurdles using the following approaches: (1) introducing defects into the Cu_2S semiconductor to form nonstoichiometric $Cu_{2-x}S$, which boosts the free carrier density for enhancing the LSP effect and advancing the conductance (Riha et al., 2011; Wang et al., 2015; Ren et al., 2017); and (2) coupled plasmonic metal and semiconductors provided with a high free carrier density with the Cu_2S semiconductor to form hybrid hetero junctions, in which the integration of noble metal and plasmonic semiconductors with Cu_2S could not only enhance the LSP field but also would be able to change and improve the electron transitions in the semiconductor domain (Zhuang et al., 2016; Deng et al., 2017; Han et al., 2016). Accordingly, in addition to the abovementioned composition optimization, Cu_2S/CdS coaxial nanowires (Pan et al., 2012), core-shell $CdS-Cu_2S$ nanorod arrays (Wong et al., 2015), hierarchically assembled $ITO@Cu_2S$ nanowire arrays (Jiang et al., 2015), and hollow-structured $CuS@Cu_2S@Au$ nanohybrids (Deng et al., 2017) were designed to enhance the charge collection and light trapping as well as to improve the charge transport by structural optimization, which further boosts performance and promotes application in electronic and photoelectronic devices (Wong et al., 2015; Jiang et al., 2015; Pan et al., 2012). Significantly, the current research on low-angle-dependent or thermal-assisted photoelectronic effects are rare, which further limits advances in performance and hinders their use in practical applications (Saran and Curry, 2016). The reason is that it is a great challenge to fabricate low-angle-dependent optical and photoelectronic devices with omnidirectional light absorption properties by artificial preparation, despite findings showing that various Cu_2S nanostructures offer many advantages as candidates for electronic and photoelectronic applications with the development of good preparation techniques (Wong et al., 2015; Jiang et al., 2015; Pan et al., 2012; Liu et al., 2010). In addition, a superheating phenomenon arises during high dark current and excessive electron-hole recombination, thereby hindering thermal-assisted applications in electronic and photoelectronic devices.

One way to overcome the above-mentioned limitations is to boost the free carrier density of Cu_2S film to enhance the LSP effect and advance the conductance while constructing a hierarchically micro-nano structure with omnidirectional light absorption and temperature auto-regulation characteristics. Recently, these Cu_2S films have been prepared using gas-state reaction (Martinson et al., 2013; Carbone et al., 2011), solid-state reaction (Manzi et al., 2015; Liu et al., 2010), and solution processes (Jiang et al., 2015; Zhuang et al., 2016; Yu et al., 2018; Deng et al., 2017). However, most of these preparation methods have poor control of the stoichiometry and construction of their extraordinarily fine functional structures (Yu et al., 2018; Yao et al., 2011). Moreover, especially for most gas-state and solid-state reactions, these reactions are energy-intensive and are performed using ultra-high-vacuum-solid-state techniques and valuable equipment, resulting in high fabrication cost (Riha et al., 2011). Encouragingly, with the recent development of nanotechnology, research on biomaterials, bio-inspired materials, and biomimetic materials has expanded to the micro- and nano-scales, which has led to a big breakthrough in the design of advanced functional materials (Yao et al., 2011; Zhang et al., 2015; Yu et al., 2013a; Liu et al., 2020; Tian et al., 2015b, 2021). Herein, inspired by the geological processes, this study presents an effective method for preparing a type of $Cu_{1.97}S/Cu_2S$ micro/nano-structure film containing a solid solution Au, which is invisible in the X-ray diffraction (XRD) pattern ("invisible" Au: a solid solution Au whose diffraction peaks are invisible in the XRD pattern), with bio-inspired omnidirectional light absorption and temperature auto-regulation characteristics (Au-$Cu_{1.97}S/Cu_2S$-C-T_FW) for multifunctional photoelectric applications. Here nanotechnology is combined with biomimetic technology to circumvent the limitations of the current preparation methods. To the best of our knowledge, the thermal-assisted photoelectric detection properties of these Cu_2S nanoparticles (NPs) systems have rarely been explored. Moreover, the solid solution metal atom enhancement has seldom been applied to photodetection. This study introduces the possibility of producing the thermal-assisted photoelectric application, and it suggests that the Au-$Cu_{1.97}S/Cu_2S$-C-T_FW can be a new class of low-cost, room-temperature photoelectric detectors. This effort shows that the concept of photo-heating can be used to enhance photoelectric detection by passive radiative balance. Furthermore, this strategy offers a new direction for preparing thermally stable solid solution metal atoms and copper chalcogenide systems with enhanced LSP effects and advanced conductance properties for photoelectric applications.

RESULTS AND DISCUSSION

Preparation of Au-$Cu_{1.97}S/Cu_2S$-C-T_FW

The primary procedure for fabricating Au-$Cu_{1.97}S/Cu_2S$-C-T_FW is shown in Figure 1. First, the black forewing of the *T. helena* butterfly (T_FW) was chosen as a biomimetic template; it has a sophisticated micro-nano functional structure (SMNFS) (Figures 2A, 2B, and S1) with omnidirectional light absorption and
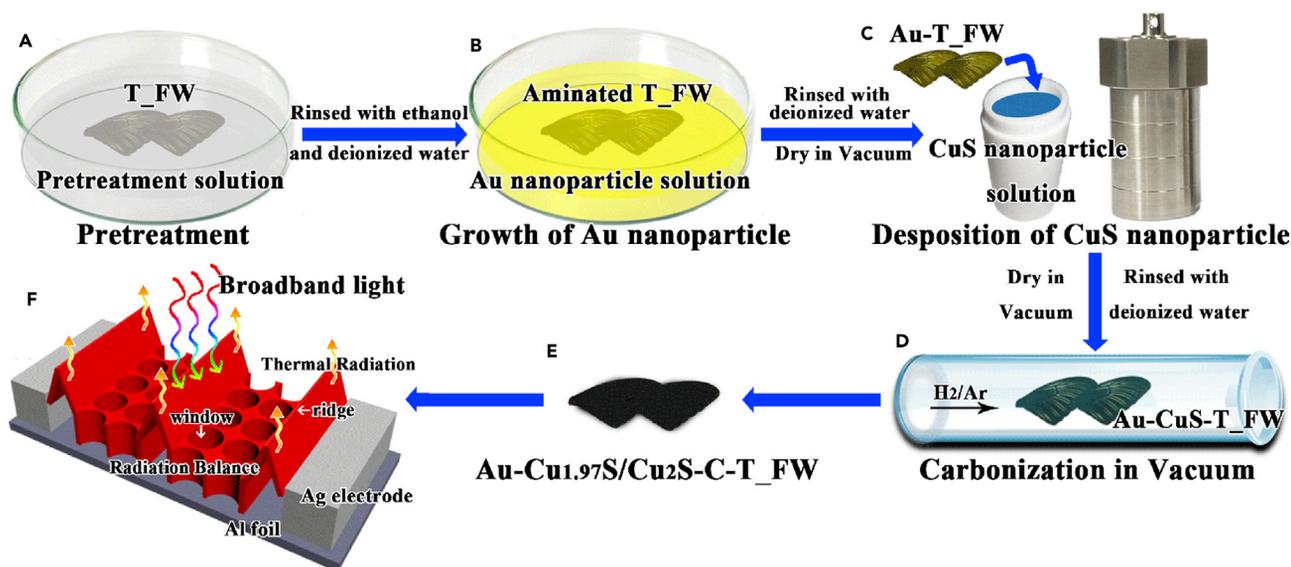
Figure 1. Schematics of the preparation process
Schematic of the preparation process for Au-Cu$_{1.97}$S/Cu$_2$S-C-T_FW and Au-Cu$_{1.97}$S/Cu$_2$S-C-T_FW photodetectors.

temperature auto-regulation characteristics (Tian et al., 2015a; Zhao et al., 2011; Wang et al., 2014; Berthier, 2005; Herman et al., 2011). Then, the T_FW are pretreated and aminated before the Au NPs are deposited on the surface of the sophisticated micro-nano functional structure of T_FW (Au-T_FW) by electroless deposition. Next, the CuS NPs are deposited on the surface of the Au-T_FW (Au-CuS-T_FW) by the hydro-thermal method (Tian et al., 2015a). During this step, stable stoichiometric CuS NPs are prepared using a low-cost solution process, in which the poorly controlled stoichiometry for Cu$_2$S synthesis is circumvented because the preparation of stable stoichiometric CuS NPs is easier and costs less compared with the prep-aration process used for stable stoichiometric Cu$_2$S NPs (Tian et al., 2015a). Because of the efficient reduc-ibility of H$_2$, an innovative low-concentration-ratio H$_2$ reduction method is used successfully to reduce the stoichiometric CuS NPs into completely reduced stoichiometric Cu$_2$S. Here, Au-CuS-T_FW is placed in the hot center of the tube furnace vented with 5:95 H$_2$/Ar mixture gases at 50 sccm. The furnace is gradually heated from room temperature to 450°C at a rate of 7.5°C/min, and then the chamber is maintained at 450°C for 120 min. During this procedure, first, with inspiration from the geological processes leading to the formation of sulfide ores that often result in the precipitation of gold-bearing sulfide, which can contain high concentrations of this metal in an "invisible" state, the Au starts to become "invisible" by the formation of isomorphous solid solution when the temperature rises to 120°C, and the "invisible" Au concentration grows with increasing temperatures from 120°C to 450°C (Tagirov et al., 2016). Then the CuS begins to be reduced by H$_2$ when the temperature is greater than ~433°C, and the following reaction takes place: $2CuS + H_2 \rightarrow Cu_2S + H_2S$ (Habashi and Dugdale, 1973), which forms the "invisible" Au-Cu$_2$S system. Even-tually, the "invisible" Au either substitutes for Cu in the Cu$_2$S lattice, or it is incorporated into the Cu$_2$S ma-trix without distortions of the cationic sublattice that Au exists in the form of the isomorphous solid solution and is invisible in the XRD pattern-formed "invisible" state, which boosts the internal electron concentra-tion of the system and forms the positively charged Au centers to elevate the performance of the Cu$_2$S film (Tagirov et al., 2014, 2016; Yang et al., 2013; Jiang et al., 2019; Qiao et al., 2011; Wei et al., 2014). Corre-spondingly, the easier diffusion characteristics of the H$_2$/Ar mixture gases not only provide a more efficient reduction performance at both the surface and interior domains of CuS film but also effectively prevent the injection of the extra component when compared with the reported reduction methods by injecting a strong reducing agent to drive the reduction of Cu^{2+} to Cu$^+$ (Deng et al., 2017; Kriegel et al., 2012). Signif-icantly, this strategy offers a new direction for preparing the thermally stable solid solution metal atoms on photoelectric supports, thereby overcoming the faults of single metal atoms that can be mobile and aggre-gate into NPs on supports (Jiang et al., 2019; Jones et al., 2016). Meanwhile, the chitin-matrix template (T_FW) has been carbonized to enhance the infrared absorption during this sintering process (Tian et al., 2015c). Here, the carbon-matrix Cu$_2$S films containing "invisible" Au with bio-inspired omnidirectional light absorption and temperature auto-regulation characteristics are ultimately achieved
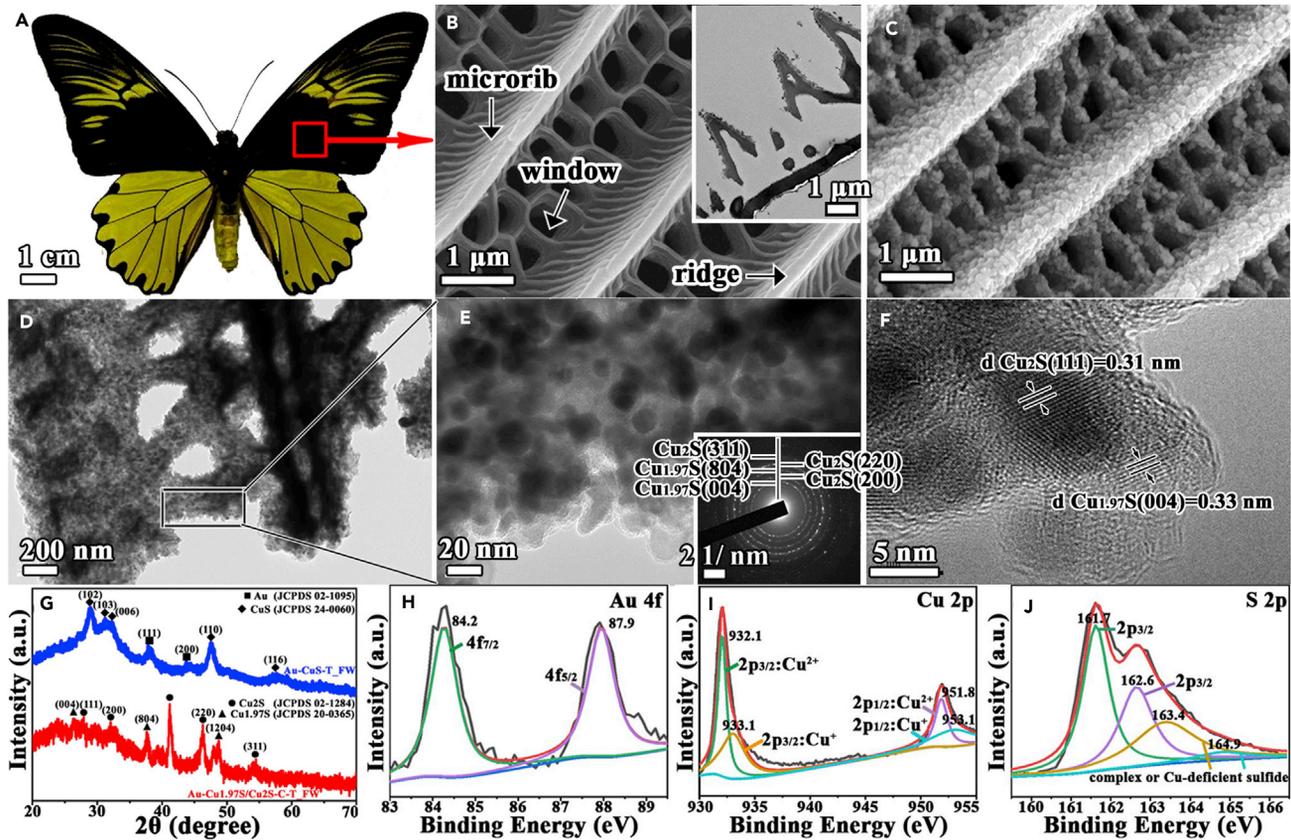
Figure 2. Characterization of Au-Cu$_{1.97}$S/Cu$_2$S-C-T_FW

(A) Digital photograph of *T. helena*.

(B) SEM image of T_FW. The inset is the TEM image of the cross-section of T_FW.

(C) SEM image of Au-Cu$_{1.97}$S/Cu$_2$S-C-T_FW.

(D–F) TEM and high-resolution TEM images of Au-Cu$_{1.97}$S/Cu$_2$S-C-T_FW, respectively. The inset of (E) is the SAED pattern of Au-Cu$_{1.97}$S/Cu$_2$S-C-T_FW.

(G) XRD results of Au-CuS-T_FW and Au-C$_{1.97}$S/Cu$_2$S-C-T_FW.

(H–J) XPS spectra of (H) Au 4*f*, (I) Cu 2*p*, and (J) S 2*P* regions for Au-C$_{1.97}$S/Cu$_2$S-C-T_FW.

(Au-Cu$_2$S-C-T_FW). Last, because the stoichiometric Cu$_2$S NPs are prone to oxidation into more thermodynamically stable and nonstoichiometric copper chalcogenide phases containing both Cu$^+$ and Cu^{2+} ions, when the Au-Cu$_2$S-C-T_FW film is exposed to air under ambient conditions, the Cu$_2$S NPs located at the surface of the Au-Cu$_2$S-C-T_FW film are transformed in the thermodynamically stable nonstoichiometric Cu$_{1.97}$S phase (Au-Cu$_{1.97}$S/Cu$_2$S-C-T_FW) spontaneously, which forms a protective layer and boosts the free carrier density of Cu$_2$S film to enhance the LSP effect and advance conductance (Kriegel et al., 2012; Riha et al., 2011). The detailed experimental procedure is presented in the Experimental section of Supplemental information. With benefits from the unique features of Au-Cu$_{1.97}$S/Cu$_2$S nano-composites and the bio-inspired characteristics of T_FW, the Au-Cu$_{1.97}$S/Cu$_2$S-C-T_FW achieves the enhancement resulting from solid solution metal atoms and photothermal-assist in photoelectric application that exhibits an excellent low-angle-dependent photodetection property.

According to the couple effect between the melanin/chitin composite and the light trapping structure, the forewing of *T. helena* (T_FW) appears black and exhibits light absorption characteristics (Figure 2A), and it has attracted extensive interest (Tian et al., 2015a, 2015c; Zhao et al., 2011). The light trapping structure of T_FW has been characterized by scanning electron microscopy (SEM) and transmission electron microscopy (TEM) (Figure 2B and its inset). The omnidirectional, broadband absorption and temperature auto-regulation characteristics of T_FW are discussed in the Supplemental information (Figures S1–S3 and Table S1). These results demonstrate that T_FW with SMNFS has both good absorption (omnidirectional and broadband absorption) and effective emissivity to achieve temperature auto-regulation (Herman et al., 2011). The typical morphologies of Au-Cu$_{1.97}$S/Cu$_2$S-C-T_FW are shown in Figures 2C–2F,

showing that the surface of SMNFS of T_FW were coated uniformly with Au-Cu$_{1.97}$S/Cu$_2$S NPs. Evidently, the SMNFS of T_FW are well retained. The diameter measurements of Au-Cu$_{1.97}$S/Cu$_2$S NPs are shown in Figure S4 and Table S2. In addition, the high-resolution TEM images of Au-Cu$_{1.97}$S/Cu$_2$S-C-T_FW are displayed in Figures 2E and 2F. In the inset of Figure 2E, the selected area electron diffraction (SAED) pattern indicates that the combined Au-Cu$_{1.97}$S/Cu$_2$S NP system is a polycrystal-line specimen. These diffraction rings are indexed to the (004) and (804) planes of the Cu$_{1.97}$S (JCPDS no. 20-0365) and the (200), (220), and (311) planes of the Cu$_2$S (JCPDS no. 02-1284) respectively, which also corresponds to the XRD result shown in Figure 2G. The distances of 0.31 and 0.33 nm are consistent with the *d*-spacing of the (111) crystallographic plane of Cu$_2$S and the (004) crystallographic plane of Cu$_{1.97}$S, respectively (Figure 2F).

The "invisible" Au present in Cu$_2$S in the form of an isomorphous solid solution and the stabilization of Au-Cu$_{1.97}$S/Cu$_2$S-C-T_FW are investigated here by means of XRD analysis. As displayed in Figure 2G, the XRD pattern of Au-CuS-T_FW confirms that the stoichiometric Au-CuS combination NP system has been prepared (trigonal-structured CuS: JCPDS no. 24-0060, cubic phase of Au: JCPDS no. 02-1095) (Tian et al., 2015a). Moreover, as exhibited in the XRD pattern of Au-Cu$_{1.97}$S/Cu$_2$S-C-T_FW, after the Au-Cu$_2$S-C-T_FW was initially exposed to air for 5 months, the diffraction peaks with 2-theta values of 26.2°, 37.6°, and 48.6° were assigned to the (004), (804), and (1204) planes of the orthorhombic-structured Cu$_{1.97}$S, respectively (JCPDS no. 20-0365), and diffraction peaks with 2-theta values of 27.8°, 32.1°, 46.2°, and 54.5° were assigned to the (111), (200), (220), and (311) planes of the cubic-structured Cu$_2$S, respectively (JCPDS no. 02-1284) (Liu et al., 2013; Kriegel et al., 2011). As a result, the XRD pattern confirmed that the Cu$_2$S NPs located at the surface of the Au-Cu$_2$S-C-T_FW are transformed to the thermodynamically stable nonstoichiometric Cu$_{1.97}$S phase and form a protective layer for stabilizing the Au-Cu$_{1.97}$S/Cu$_2$S-C-T_FW. Furthermore, the initial exposure of Au-Cu$_2$S-C-T_FW to air for 5 months demonstrates that Au-Cu$_{1.97}$S/Cu$_2$S-C-T_FW achieves remarkable stabilization. Herein, the oxidation of Cu$_2$S and the stabilization of Cu$_{1.97}$S/Cu$_2$S can be ascribed to the following process. First, upon exposure to the air, the surface Cu$^+$ oxidizes to Cu^{2+}. Meanwhile, it establishes a chemical potential gradient, thereby resulting in the diffusion of Cu$^+$ from the NP core to the surface. Then, a more thermodynamically stable nonstoichiometric Cu$_{1.97}$S is obtained, and equilibrium is achieved (Riha et al., 2011). In addition, during oxidation process, the decreased Cu combines with O, which forms the Cu$_2$-O-S phase.[16-18] However, as shown in electron energy loss spectroscopy (EELS) analysis (Figure S5), the quantity of O element is very small, which demonstrates that there is very little Cu$_2$-O-S phase in Au-Cu$_{1.97}$S/Cu$_2$S-C-T_FW. Thus, the Cu$_2$-O-S phase is reasonably ignored in our work and the reported researches about Cu$_{2-x}$S nanocrystals.[16, 19-21] Of interest, as shown in EELS analysis of Au-Cu$_{1.97}$S/Cu$_2$S-C-T_FW (Figure S5), there are evident Au distributed in the Au-Cu$_{1.97}$S/Cu$_2$S-T_FW, but the Au diffraction peaks are invisible in the XRD pattern of Au-Cu$_{1.97}$S/Cu$_2$S-C-T_FW (Figure 2G). In addition, compared with the XRD pattern of Cu$_{1.97}$S/Cu$_2$S-C-T_FW (Figure S6) that was fabricated using the same preparation process as that of Au-Cu$_{1.97}$S/Cu$_2$S-C-T_FW except for the step in which Au NPs are deposited on the surface of the sophisticated micro/nano functional structure of T_FW, the XRD patterns of Au-Cu$_{1.97}$S/Cu$_2$S-C-T_FW do not exhibit obvious differences. This result demonstrates that the Au is "invisible" and the crystalline structure of Cu$_2$S is changeless, which indicates that the "invisible" Au is present in the form of the isomorphous solid solution formed by substitution with Cu atoms (Tagirov et al., 2016). Additionally, according to the XRD pattern of Cu$_{1.97}$S/Cu$_2$S-C-T_FW, we can also conclude that the Cu$_2$S NPs located at the surface of Cu$_2$S-C-T_FW are transformed during the thermodynamically stable nonstoichiometric Cu$_{1.97}$S phase and form a protective layer for stabilizing the Cu$_{1.97}$S/Cu$_2$S-C-T_FW.

Furthermore, a systematic X-ray photoelectron spectroscopy (XPS) study was performed to investigate the "invisible" Au as well as the chemical composition and the valence states of both the Cu and S atoms in the Au-Cu$_{1.97}$S/Cu$_2$S-C-T_FW. As shown in Figure 2H, the XPS spectra of the Au 4*f* regions are evident, and the gold peaks are identified clearly, although the Au is invisible in the XRD pattern. Moreover, compared with the XPS spectra of Au NPs reported by Ding et al (Ding et al., 2014), the XPS spectra of the Au 4*f* for Au-CuS-T_FW are left-shifted (Figure S7A), which indicates a possible electron transfer from Au NPs to CuS NPs in Au-CuS-T_FW (Tian et al., 2015a; Ding et al., 2014). The similar left shift also suggests a possible electron transfer from Au atoms to Cu$_2$S or Cu$_{1.97}$S matrixes in Au-Cu$_{1.97}$S/Cu$_2$S-C-T_FW, which confirms the presence of Au atoms with a partially positive charge (Tian et al., 2015a; Tagirov et al., 2016; Jiang et al., 2019; Qiao et al., 2011; Ding et al., 2014). As depicted in Figure 2I, the Cu 2*p* XPS spectra contain a mixture of Cu$^+$ and Cu^{2+}, which shows oxidation from Cu$^+$ to a mixture of Cu$^+$ and Cu^{2+} when exposing the initial Au-Cu$_2$S-C-T_FW to air (Riha et al., 2011; Conley et al., 2014). Furthermore, in contrast with the Cu 2*p$_{3/2}$* and Cu 2*p$_{1/2}$*
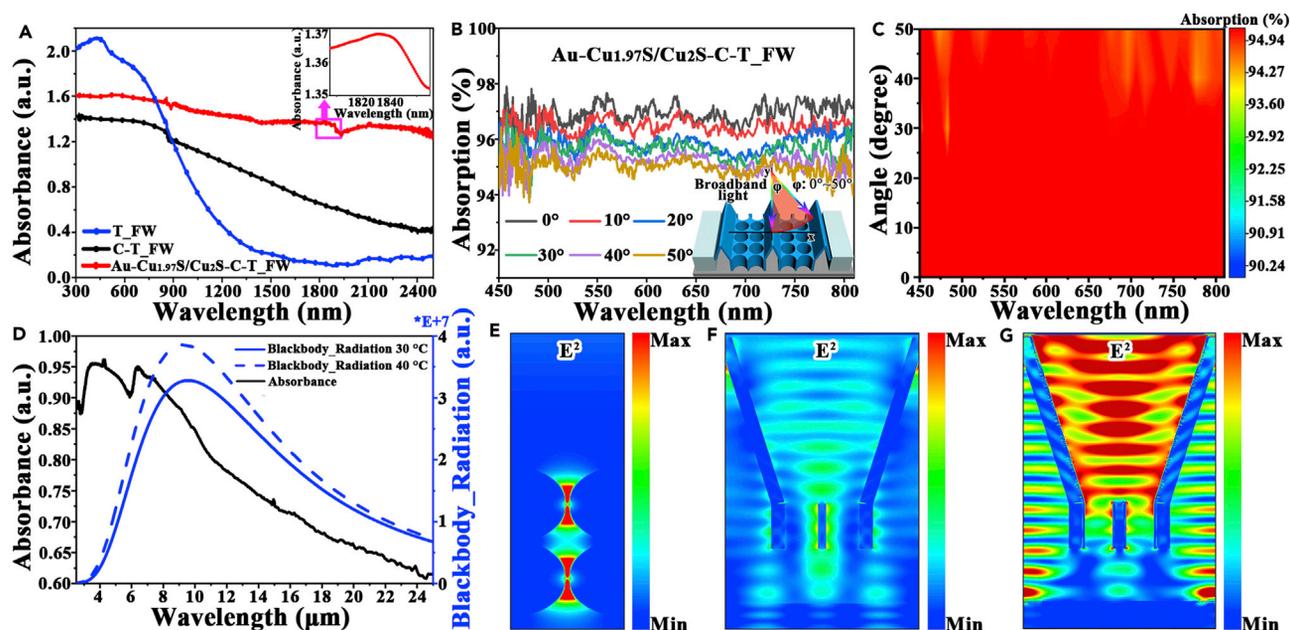
Figure 3. Absorption and thermal radiation analysis

(A–G) (A) The absorption spectra of T_FW, C-T_FW, and Au-Cu$_{1.97}$S/Cu$_2$S-C-T_FW over a wavelength range from 300 to 2,500 nm. The insert is the absorption spectra of Au-Cu$_{1.97}$S/Cu$_2$S-C-T_FW over a wavelength range from 1,795 nm to 1,870 nm; (B) angle-dependent absorption of Au-Cu$_{1.97}$S/Cu$_2$S-C-T_FW over a wavelength range from 450 to 810 nm. The incident angles increase from 0° to 50°. The insert is a schematic illustration of the incidence at different angles of the photodetector; (C) filled contour plot of angular dependence versus wavelength; (D) the absorption spectra and blackbody radiation at temperatures of 30°C and 40°C for Au-Cu$_{1.97}$S/Cu$_2$S-C-T_FW over a wavelength range from 2.5 to 25 μm; (E–G) the FDTD simulation of $\left|\vec{E}\right|^2$ intensity distribution maps of (E) Cu$_2$S-NPs, (F) C-T_FW, and (G) Cu$_2$S-C-T_FW. The wavelength of the incident light in the FDTD simulation is fixed at 808 nm.

peaks of the Au-CuS-T_FW that are narrow and devoid of satellite peaks, the Cu 2$p_{3/2}$ and Cu 2$p_{1/2}$ peaks of the Au-Cu$_{1.97}$S/Cu$_2$S-C-T_FW are right-shifted and broadened (Figure S7C). Additionally, after undergoing splitting, the pronounced Cu$^+$ satellite peaks are formed (Figure S7C). These results indicate a possible electron transfer from Cu$_{1.97}$S to Cu$_2$S. Here, the Cu$^+$ satellite peaks can be attributed to the factor in which the surface Cu$^+$ oxidizes to Cu^{2+}, forming a surface oxide because XPS is primarily a surface characterization technique (Riha et al., 2011). For S, the XPS spectra of S 2P regions are described in detail by deconvolution in subcomponents (Figure 2J). Here, there are two primary S 2$p_{3/2}$ component peaks positioned at 161.7 and 162.6 eV, and they are ascribed to sulfides and disulfides, respectively, indicating the partial oxidation of the S species (Han et al., 2016). In addition, the other two peaks positioned at 163.4 and 164.9 eV can be referenced as complexes containing elemental sulfur or Cu-deficient nonstoichiometric sulfides (Tian et al., 2015a; Han et al., 2016). Moreover, compared with the sulfide peak of Au-CuS-T_FW positioned at 161.0 eV (Figure S7B), the sulfide peak of Au-Cu$_{1.97}$S/Cu$_2$S-C-T_FW emerges at 161.7 eV (Figure S7D). The shift in the sulfide peak can be attributed to the decrease in the average length of the Cu-S bond by oxidation (Han et al., 2016).

Absorption and thermal radiation

To further explore the possibility of using the as-fabricated Au-Cu$_{1.97}$S/Cu$_2$S-C-T_FW as a broadband photodetection material, the broadband, omnidirectional, high-efficiency absorbance and thermal radiation of the Au-Cu$_{1.97}$S/Cu$_2$S-C-T_FW are discussed in Figure 3. As depicted in Figure 3A, the carbon matrix T_FW exhibits enhanced near-infrared (NIR) absorption compared with T_FW, which is consistent with previous reports (Zhao et al., 2011; Tian et al., 2015c). Moreover, in Figure 3A, Au-Cu$_{1.97}$S/Cu$_2$S-C-T_FW exhibits a more significant broadband photoabsorption performance (300–2,500 nm). Additionally, the absorption pattern of Au-Cu$_{1.97}$S/Cu$_2$S-C-T_FW shows another typical behavior of the plasmonic feature in Cu$_{1.97}$S NPs that shows a pronounced LSP band centered at approximately 1,830 nm (inset of Figure 3A), which is highly consistent with the report by Kriegel et al. (2012). The absorption peak of plasmonic feature Au-Cu$_{1.97}$S/Cu$_2$S-C-T_FW demonstrates that the number of free carriers (copper vacancies) on Cu$_{1.97}$S are increased, which gives rise to a higher free carrier absorption, wherein the high concentration of free carriers in Cu$_{1.97}$S NPs similar to electrons in plasmonic metal NPs leads to LSPs (Kriegel et al., 2012).

Furthermore, to expand the discussion on efficient broadband photoabsorption, a finite difference time domain (FDTD) simulation method is carried out. The detailed descriptions and schematic diagrams for the FDTD simulation are provided in the Supplemental information and in Figure S8. On the one hand, compared with the absorption of Cu_2S-NPs (without HASAS), the Cu_2S-C-T_FW (with SMNFS) shows an enhanced photoabsorption clearly, as depicted in the simulation results (Figure S9). Additionally, as shown in Figures 3F and 3G, the intensive electromagnetic field energy flux density (EFEFD) is present between every two ridges and in the windows, which demonstrates that the triangular roof-type ridges are good at focusing incident light into the scale interior, and the windows elongate the effective light path and the energy density distribution interspace efficiently (Tian et al., 2015a, 2015c). These results indicates that the SMNFS of C-T_FW contributes an important factor for broadband photoabsorption (Tian et al., 2015a, 2015b, 2015c; Zhao et al., 2011). On the other hand, from Figure 3E, we observe that the substantially enhanced EFEFDs are located in the adjacent region between two Cu_2S NPs and the adjacent region between two layers of Cu_2S NPs, which indicate that the coherent coupling between adjacent systems can enhance the interplay between the incident light and the material promoting the photoabsorption. Moreover, on comparing Figure 3F with Figure 3G, except for the intensive EFEFDs that are present between every two ridges and in the windows, there are obvious electromagnetic field hotspots situated on the surface of the ridges on the Cu_2S-C-T_FW coated by Cu_2S NPs, which are attributed to coherent couplings between adjacent systems. Consequently, from the measurement and simulation results, we can conclude that the efficient broadband photoabsorption performance of Au-$Cu_{1.97}S$/Cu_2S-C-T_FW is attributed to the plasmon and the coherent coupling between adjacent resonant systems of Au-$Cu_{1.97}S$/Cu_2S that synergistically combine with the SMNFS (Tian et al., 2015a). Additionally, given the nano hole window structure with antireflection ridges that produce an omnidirectional light absorption feature (Wang et al., 2014), the Au-$Cu_{1.97}S$/Cu_2S-C-T_FW exhibits an omnidirectional broadband (from 450 to 810 nm) and high-efficiency absorption performance (Figures 3B and 3C). As shown in Figures 3B and 3C, as the incidence angle is increased from 0° to 50°, the average absorption of the Au-$Cu_{1.97}S$/Cu_2S-C-T_FW gradually decreases from 96.93% to 95.01%, which exhibits an approximate linear relationship between the absorption and the angle (Figure S10A). Compared with the average absorptance at the vertical incidence (0°), the reduction rate of the average absorption at the incident angles of up to 50° is only 1.929% (Figure S10B). Such a low reduction rate and high absorbance demonstrate that Au-$Cu_{1.97}S$/Cu_2S-C-T_FW achieves a high-efficiency, low-angle-dependent and broadband photoabsorption that profits from the SMNFS of T_FW. Valuably, as depicted in Figure 3D, the Au-$Cu_{1.97}S$/Cu_2S-C-T_FW also reveals several strong absorbance peaks at 4.26, 6.39, and 7.47 μm, which predicts the spectral emissivity of Au-$Cu_{1.97}S$/Cu_2S-C-T_FW, because Kirchhoff's law states that emission is equal to absorption (Arpin et al., 2013). Herein, the thermal radiation peaks centered on the 6.39 and 6.48 μm positions at the edge of the blackbody radiation for 40°C, in which the emissivity stays at a relatively constant value up to 40°C and increases beyond this, thereby playing a key role as the thermal regulator (Berthier, 2005; Herman et al., 2011). Accordingly, the radiation regulation plays a key role as a thermal regulator that modulates the energetic balance to prevent overheating and achieves temperature auto-regulation. Consequently, except for the low-angle-dependent and omnidirectional broadband high-efficiency absorption feature inherited from T_FW, the Au-$Cu_{1.97}S$/Cu_2S-C-T_FW also inherits the temperature auto-regulation by radiative balance, which offers a significant advantage to overcome the hurdles to then promote the Cu_2S nanostructures as candidates for electronic and photoelectronic applications, especially for thermal-assisted photoelectronic applications.

Broadband photodetection

To analyze the broadband photoresponse characterizations of Au-$Cu_{1.97}S$/Cu_2S-C-T_FW covering the visible (VIS) and NIR, the time-dependent response curves were measured at room temperature under ambient conditions. Herein, the as-fabricated devices with Au-$Cu_{1.97}S$/Cu_2S-C-T_FW as the channel and Ag paste as contact are used for the broadband photodetector. As shown in Figures 4A–4C, the photocurrent of the Au-$Cu_{1.97}S$/Cu_2S-C-T_FW photodetector at a 0.5 V bias potential exhibits a steady increase with increasing illumination power from 0.06 to 1.67 mWmm^{-2}. At the relatively higher power densities (>0.56 mWmm^{-2}), when the light is turned on, the photocurrent increases sharply at the beginning, and the photocurrents exhibit lower growth at the later stages. The opposite findings occur when the light is turned off. Moreover, compared with the slowly increasing process of photocurrent illuminated by 660 nm light, the slowly increasing processes of photocurrent illuminated by 808 and 980 nm light are much slower. However, at low power densities (<0.11 mWmm^{-2}), the photocurrent only exhibits the sharply increasing/decreasing process when the light is turned on/off, and there is a lack of the slowly increasing/decreasing process at the end. The reasons are that the sharp photocurrent increases/decreases arise from the photoelectric
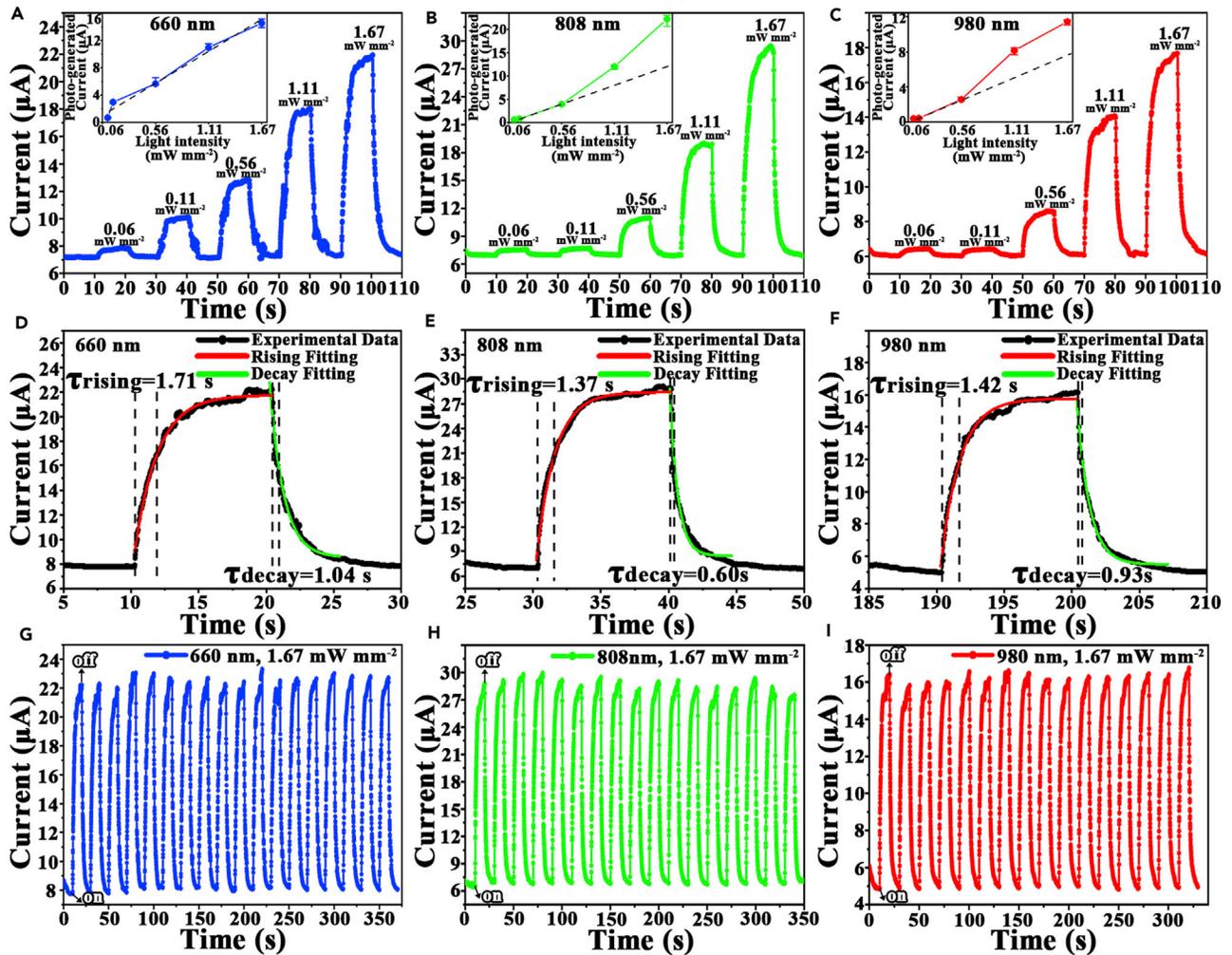
Figure 4. Photodetection analysis

(A–C) Time-dependent photocurrent response of Au-Cu$_{1.97}$S/Cu$_2$S-C-T_FW photodetector under switched-on/off light (660 nm, 808 nm, and 980nm) with different power levels (0.06–1.67 mWmm^{-2}) at a 0.5 V bias voltage. The insets are the power-dependent peculiarity of the photocurrent under different incident light wavelengths (660, 808, and 980 nm).

(D–F) The response speed under different incident light wavelengths (660, 808, and 980 nm).

(G–I) The photoresponse cycle stabilities under different incident light wavelengths (660, 808, and 980 nm). These tests were performed at room temperature (20°C), and the bias was 0.5 V.

effect generated photoinduced carriers, and the slowly increasing/decreasing process profits from the photothermal effect contributed by the LSPs of Au-Cu$_{1.97}$S/Cu$_2$S and the electron transitions in the semiconductor domain (Deng et al., 2017; Kriegel et al., 2012; Luther et al., 2011). For further comparison, as revealed in Figures 4A–4C and their insets, under increased illumination power, the photocurrent increased. Additionally, there is an approximately linear relationship between the photocurrents and the illumination power density at the low power densities (<0.11 mWmm^{-2}), which suggests that the photocurrent is dominated by the conversion of single photons to singe electrons over this range of incident light intensities (Knight et al., 2011), and it also demonstrates that the photocurrent primarily arises from the photoelectric effect. When further increasing the incident power, the photocurrents deviate from the linear relationship. In particular, compared with the photocurrent illuminated by 660 nm light, the photocurrents illuminated by 808 and 980 nm incident light displayed a greater deviation from the linear dependence (the insets of Figures 4A–4C). These results further demonstrate that there are photothermal effect-assisted photoelectric effects which boost the carrier concentration and promote the carrier transmission to improve the photoelectric effects. Furthermore, as shown in Figure S11, there was a clear temperature increasing process when the light was turned on at the same laser power density (1.67 mWmm^{-2}) as a

temporal photo response test, which evidently demonstrates that the photoelectric effect on the photo response is accompanied by photothermal effects. Significantly, with incident laser power as low as 0.06 mW mm^{-2}, the Au-Cu$_{1.97}$S/Cu$_2$S-C-T_FW photodetector still exhibits a clear photoresponse for the incident wavelengths of 660, 808, and 980nm (Figures 4A–4C). Moreover, to quantify the photoresponse performance of the devices, the spectral responsivity (R_λ) and detectivity ($D*$) are discussed to evaluate the ability to convert the light signals into electrical signals and measure the detector sensitivity under a certain wavelength at a 0.5 V bias. Here, R_λ and $D*$ are defined as (Xie et al., 2017)

$$R_\lambda = (I_{on} - I_{off})/PS \qquad \text{(Equation 1)}$$
$$D* = R_\lambda / (2qI_d/S)^{1/2} \qquad \text{(Equation 2)}$$

where P refers to the incident light intensity and S is the effective area under illumination (here S is approximately 0.5 mm^2), I_d is the dark current, and q is the absolute value of the electron charge (1.6×10^{-19} C) (Deng and Li, 2014). For 660, 808, and 980 nm light illumination under a light intensity of 1.67 mW mm^{-2} at a 0.5 V low bias voltage, the R_λ and $D*$ of the Au-Cu$_{1.97}$S/Cu$_2$S-C-T_FW detectors are estimated to be 17.36, 26.37, and 13.40 mA W^{-1}, corresponding to $D*$ of 7.79×10^7, 1.25×10^8, and 7.71×10^7 Jones, respectively. All the obtained parameters are listed in Table S3. These parameters are comparable and even higher than those for most reported photodetectors, such as the reported few-layer group-VIB transition-metal dichalcogenides p-n photodiode (WSe$_2$ p-n junction) which recently emerged as an interesting candidate for optoelectronic application with a responsivity of 16 mA W^{-1} (<750 nm) (Koppens et al., 2014). Reasonably, according to Equations 1 and 2, if replacing the Ag paste contacts process with photolithography and oxygen plasma etching processes, the S diminishes from 0.5 mm × 1 mm to 8 μm × 30 μm, as reported (Yu et al., 2013b). Consequently, the R_λ and $D*$ increase by four and two orders of magnitudes, respectively, which are very competitive for the R_λ and $D*$ values of current high-performance photodetectors (Xie et al., 2017; Koppens et al., 2014; Yu et al., 2013b; Baugher et al., 2014; Youngblood et al., 2015). The response speed is also one of the critical parameters of photodetectors. In this study, the response time (τ_R) represents the time needed from the dark current increase to $1-1/e \approx 63\%$ of the maximum photocurrent, and the recovery time (τ_D) is defined as the time needed for recovery to $1/e \approx 37\%$ of the maximum photocurrent (Cao et al., 2014; Lopez-Sanchez et al., 2013). As shown in Figures 4D–4F, the fast τ_R/τ_D of the Au-Cu$_{1.97}$S/Cu$_2$S-C-T_FW photodetector for 660, 808, and 980 nm incident light wavelengths are 1.71/1.04 s, 1.37/0.60 s, and 1.42/0.93 s, respectively. Here, the τ_R/τ_D for the NIR (808, 980 nm) incident light is quickly attributed to the more efficient NIR photothermal effect, which boosts the carrier transmission. In addition, the stability is another critical factor for evaluating a practical photodetector. Here, time-resolved photoresponses are measured for multiple illumination cycles to evaluate the stability of the Au-Cu$_{1.97}$S/Cu$_2$S-C-T_FW photodetector. As depicted in Figures 4G–4I, for 660, 808, and 980 nm light illumination with 1.67 mWmm^{-2}, the current density and response speed after 17 cycles exhibit no distinct decay, and the error analysis of the photoresponse cycle stabilities are shown in Figure S12. The ultra-low errors show that the Au-Cu$_{1.97}$S/Cu$_2$S-C-T_FW photodetector have excellent stability (Figure S12). Moreover, the good stability of Cu$_{1.97}$S/Cu$_2$S-C-T_FW and Au-Cu$_{1.97}$S/Cu$_2$S-C-T_FW(20hr) photodetectors are also exhibited in Figures S13 and S14. These results demonstrate the robustness and reproducibility of our photodetector for broadband photoresponses.

To investigate the competitive photoresponse mechanism of Au-Cu$_{1.97}$S/Cu$_2$S-C-T_FW further, here, the photodetection performances of Cu$_{1.97}$S/Cu$_2$S-C-T_FW and Au-Cu$_{1.97}$S/Cu$_2$S-C-T_FW(20 h) are compared. In contrast with the photodetection performances of Cu$_{1.97}$S/Cu$_2$S-C-T_FW in which the isomorphous solid solution Au is non-existent (Figure S13 and Table S4), the Au-Cu$_{1.97}$S/Cu$_2$S-C-T_FW exhibits an approximate 1,000-fold, 1,000-fold, and an order of magnitude increase in the photocurrent, R_λ and $D*$, respectively. To examine how the isomorphous solid solution Au atoms enhance the photoelectric detection, density functional theory (DFT) calculations were further performed (Xu et al., 2012). The charge density difference distribution images (Figures 5A and 5B) reveal a stronger charge distribution at the Au-bonding region compared with the charge distribution at the Cu-bonding region, which demonstrate that the Au atom substitutes for the Cu atom, promoting a significant increase in the internal electron concentration of the system. In addition, the possible interaction is demonstrated by DFT calculations. As shown in Figures 5C and 5E, the band gap decreases when the Au atom substitutes for the Cu atom. The densities of state results reveal that the Au atom substitutes for the Cu atom arising from the hybridization between Au (d orbitals) and S (s orbitals). These experimental and DFT calculational results indicate that the "invisible" Au in Cu$_{1.97}$S/Cu$_2$S boosts the internal electron concentration of the system and forms the positively charged Au centers to elevate the conductivity, carrier transport, and electron-hole separation that
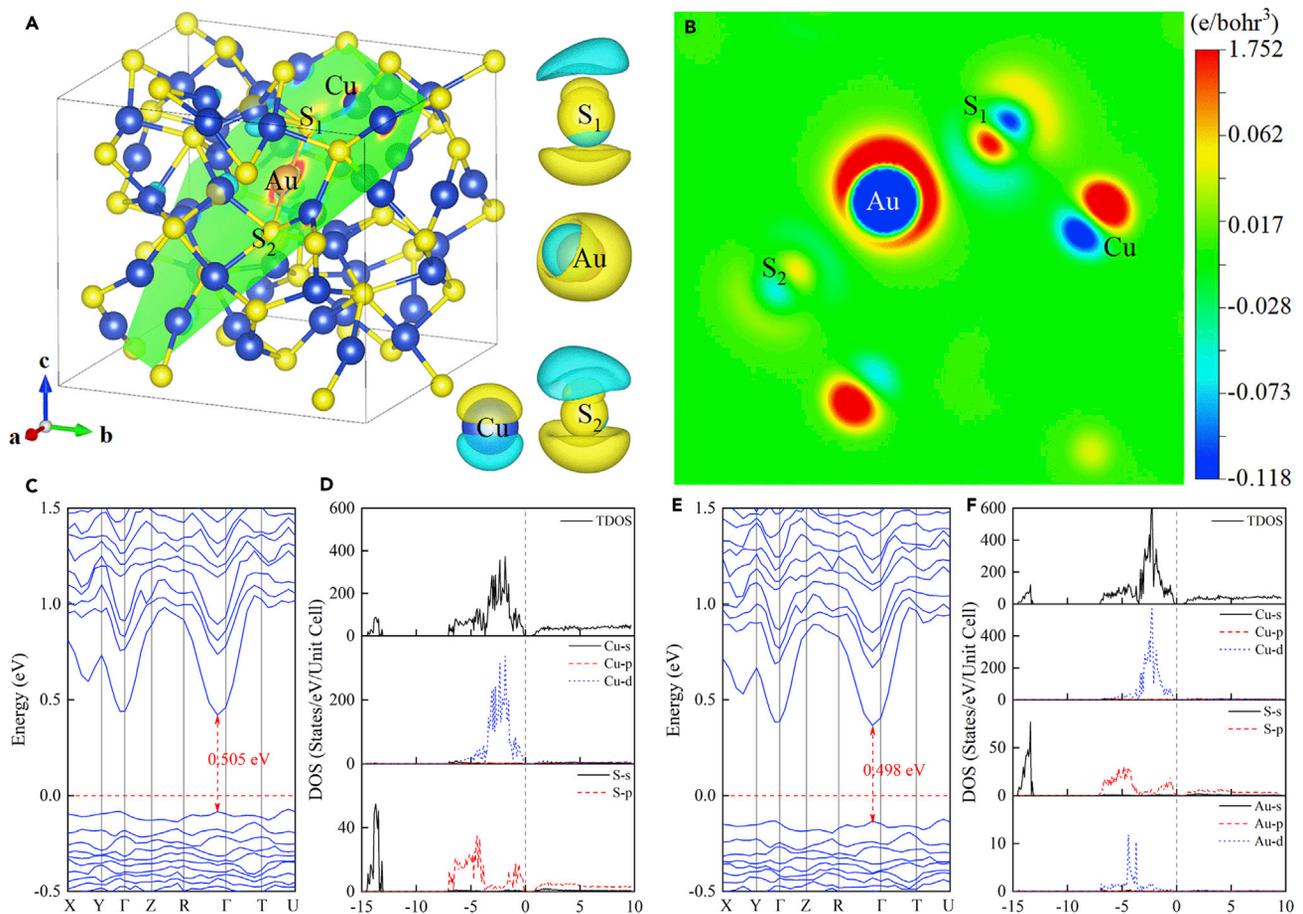
Figure 5. Density functional theory (DFT) calculations

(A–F) (A) The equilibrium crystal structure of Cu_2S in which one Cu atom is substituted by an Au atom, and the charge density difference distribution around Au, Cu, and S; (B) two-dimensional plane view of the charge density difference distribution in the cutting plane highlighted in (A); (C and E) calculated energy band structure of Cu_2S over a range from −0.5 to 1.5 eV along high symmetry paths X-Y-Γ-Z-R-Γ-T-U in the first Brillouin zones, where X (0.5, 0, 0), Y (0, 0.5, 0), Γ(0, 0, 0), Z (0, 0, 0.5), R (0.5, 0, 0), T (0, 0.5, 0.5), and U (0.5, 0.5, 0) represent the reciprocal space coordinates of special points in high symmetry directions; and (D and F) the total density of states (TDOS) and the partial density of states for the Cu, S, and Au atoms for Cu_2S in which one Cu atom is substituted by an Au atom, and the vertical dash line illustrates the Fermi energy level.

contribute to the elevated photodetection performance of Au-$Cu_{1.97}$S/Cu_2S-C-T_FW (Tagirov et al., 2014, 2016; Yang et al., 2013; Jiang et al., 2019; Qiao et al., 2011; Wei et al., 2014). Moreover, compared with the photodetection performance of Au-$Cu_{1.97}$S/Cu_2S-C-T_FW(20 h) (Figure S14 and Table S5) that does not successfully retain the SMNFS of T_FW (Figure S15), the Au-$Cu_{1.97}$S/Cu_2S-C-T_FW exhibits approximate 1,000-fold, 1,000-fold, and an order of magnitude increases in the photocurrent, R_λ and D^*, respectively. This result further indicates that the SMNFS of T_FW contributes an important factor to the broadband photoresponse.

Photothermal-assisted photodetection

Furthermore, to study the influence of thermal effects on the Au-$Cu_{1.97}$S/Cu_2S-C-T_FW photodetector, we performed a photoresponse test at different test temperatures and mapped the heat source density map, temperature map, and thermal emission map by computational simulation (Tian et al., 2015a, 2015c, 2019). The detailed descriptions of the computational simulation are provided in the Supplemental information. Here, to weaken or boost the effect from the heat effect, the test temperatures of 10°C or 38°C were selected to compare with the test under room temperature (20°C) for the natural photothermal effect. From Figures 6A and 6B, the dark current increase with the test temperature increases, which indicates that the heat effect boosts the carrier transfer. A similar tendency and a greater enhancement appeared in the photocurrent under 808 nm light illumination. The R and D^* of the photodetector were calculated
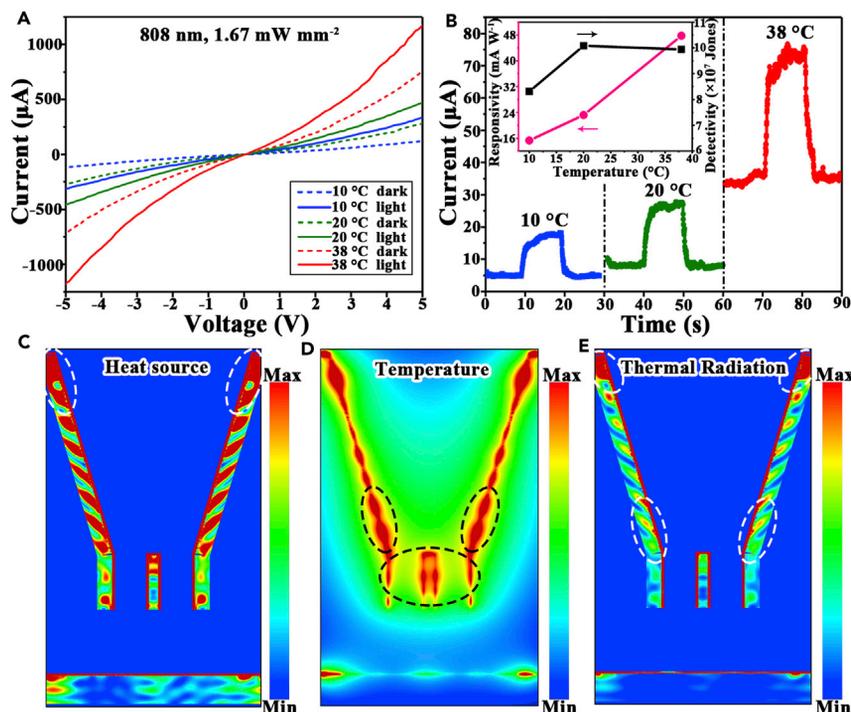
Figure 6. Thermal-assisted photodetection analysis

(A and B) (A) I-V characteristics and (B) photocurrent response of the Au-Cu$_{1.97}$S/Cu$_2$S-C-T_FW photodetector under optical irradiation (λ = 808 nm) with an incident laser power of 1.67 mW mm^{-2} under a series of testing temperatures (10°C, 20°C and 38°C, and 50°C) at 0.1 V bias voltage.

(C–E) (C) Simulated heat source intensity map, (D) simulated temperature map, and (E) simulated thermal radiation map of the Au-Cu$_{1.97}$S/Cu$_2$S-C-T_FW photodetector. The wavelength of the incident light is fixed at 808 nm.

to be 15.30 mA W^{-1}, 23.18 mA W^{-1}, and 47.74 mA W^{-1} corresponding to 8.31×10^7 Jones, 10.08×10^7 Jones, and 9.94×10^7 Jones under the test temperatures of 10°C, 20°C, and 38°C, respectively (the insert of Figure 6B). The *R* of the Au-Cu$_{1.97}$S/Cu$_2$S-C-T_FW photodetector demonstrates a steady increase when the temperature is increased. However, when the temperature rises to 38°C, the *D** values decrease weakly, because the trend in the increasing photocurrent under 808 nm light illumination (NIR, with low photon energy and the favorable photothermal characteristics) is not enough to cover the growth rate of the dark current. Under 660 nm (VIS) light illumination, the dark current, *R*, and *D** exhibit a steadily increasing trend with the increasing test temperature (Figure S16). These results demonstrate that the heat effect can promote the photoresponse by boosting electron-hole pair generation and improving the carrier transfer to advance the photocurrent, but the superheating will increase the dark current greatly and improve the electron-hole recombination, which leads to a negative effect on photodetection. To discuss the mechanism of the photothermal heat generation and thermoregulation in the Au-Cu$_{1.97}$S/Cu$_2$S-C-T_FW, the photothermal conversion and thermal radiation of the Au-Cu$_{1.97}$S/Cu$_2$S-C-T_FW can be demonstrated further by numerical simulation on the basis of the FDTD method, the Joule effect, and the thermal radiation principle (Tian et al., 2015a, 2019). To understand the photoinduced heat generation, we studied the heat source density distribution of Cu$_2$S-C-T_FW on the basis of the $\left|\vec{E}\right|^2$ intensity distribution maps (Figure 3G). As shown in Figure 6C, the heat source arises from the photothermal material (Cu$_2$S) covering the surface of the HASAS of C-T_FW. In particular, the heat source density is more intense at the region of the top of ridge, as shown in the white dashed elliptical area of Figure 6C. Moreover, the intensity of the heat source density on the surface of the windows of the SMNFS is relatively low and decreases with the increased depth of the window. However, compared with the region of the top of the ridge with a more intense heat source density, the temperature at the middle of the ridge and the windows is higher, as shown in the black dashed elliptical area of Figure 6D. This finding is consistent with the relatively lower thermal radiation strength at the middle of the ridge and the windows (Figure 6E). As shown in Figure 6E, the top and bottom of the ridges (the white dashed elliptical areas of Figure 6E) with a lower radius of curvature display stronger thermal radiation compared with the middle of ridge and the windows (Tian

et al., 2019). Consequently, Figures 6C–6E clearly exhibit the photothermal heat source, hot temperature, and thermal radiation characteristics of the SMNFS in Cu_2S-C-T_FW, which indicates that the hot temperature features result from the balance between the photothermal conversion and the thermal radiation. This finding will provide guidance for designing an effective photothermal, thermal radiation temperature auto-regulation device using less material.

Conclusion

Inspired from the geological processes, a new and innovative low-concentration-ratio H_2 reduction method is used to reduce stoichiometric Au-CuS NPs to completely reduce stoichiometric Cu_2S containing "invisible" Au, and then the thermodynamically stable Au-$Cu_{1.97}S$/Cu_2S nano-composite is formed by spontaneous oxidation. On the basis of this composite, an omnidirectional photoabsorption and thermo-regulation Au-$Cu_{1.97}S$/Cu_2S-C-T_FW film with sophisticated micro/nano functional structure is designed and fabricated as an efficient photodetector for broadband and low-angle-dependent photodetection that exhibits good performance with high responsivity (26.37 mA W^{-1}), detectivity (1.25×10^8), and good stability, which exhibit very competitive for the R_λ and D^* of the current high-performance photodetectors for which effective area is at the square-millimeter scale. The thermodynamically stable nonstoichiometric $Cu_{1.97}S$ phase forms a protective layer and boosts the free carrier density of Cu_2S film for enhancing the LSP effect and advances the conductance, which enhances the photoresponse and contributes to the film stability. Moreover, the "invisible" Au in $Cu_{1.97}S$/Cu_2S achieves the solid solution-atom enhancement, which boosts the internal electron concentration of the system and forms positively charged Au centers to elevate the conductivity, carrier transport, and electron-hole separation, thereby contributing to the elevated photodetection performance of Au-$Cu_{1.97}S$/Cu_2S-C-T_FW. Furthermore, by benefiting from the unique features of Au-$Cu_{1.97}S$/Cu_2S nano-composite and the bio-inspired characteristics of T_FW, the Au-$Cu_{1.97}S$/Cu_2S-C-T_FW can be used in the low-angle-dependent and thermal-assisted photodetection application. Here, the negative effect from the superheating involved in the thermal-assisted application is overcome by radiative balance. This effort offers a new concept for improving the stability and the photoelectric performance of copper chalcogenides. Moreover, this study opens up a new avenue toward thermoregulation and thermal-assist-enhanced properties for applications in optoelectronic and photovoltaic devices.

Limitations of the study

In this work, we offer a new concept for improving the stability and the photoelectric properties of copper chalcogenides. Moreover, it opens up a new avenue toward enhancing the performance of optoelectronic and photovoltaic devices using solid solution metal atoms and thermal-assisted, anti-overheating temperature autoregulation. Although the Au-$Cu_{1.97}S$/Cu_2S-C-T_FW photodetector presents good performance, the effective area is square-millimeter scale, which is required to reduce down to square-micron scale.

METHODS

All methods can be found in the accompanying Transparent methods supplemental file.

SUPPLEMENTAL INFORMATION

Supplemental information can be found online at https://doi.org/10.1016/j.isci.2021.102167.

AUTHOR CONTRIBUTIONS

R.Q. and J.T. performed all fabrication, characterization, simulation experiments, analysis, and wrote the manuscript. L.C. assisted with various fabrication and processing. K.X. performed the first-principles

calculation. Y.X. assisted with the first-principles calculation. All authors discussed data and commented on the manuscript.

DECLARATION OF INTERESTS

The authors declare no competing interests.

REFERENCES

Arpin, K.A., Losego, M.D., Cloud, A.N., Ning, H., Mallek, J., Sergeant, N.P., Zhu, L., Yu, Z., Kalanyan, B., Parsons, G.N., et al. (2013). Three-dimensional self-assembled photonic crystals with high temperature stability for thermal emission modification. Nat. Commun. *4*, 2630.

Baugher, B.W.H., Churchill, H.O.H., Yang, Y., and Jarillo-Herrero, P. (2014). Optoelectronic devices based on electrically tunable p-n diodes in a monolayer dichalcogenide. Nat. Nanotech. *9*, 262.

Berthier, S. (2005). Thermoregulation and spectral selectivity of the tropical butterfly Prepona meander: a remarkable example of temperature auto-regulation. Appl. Phys. A. *80*, 1397–1400.

Cao, J., Wang, Z., Zhan, X., Wang, Q., Safdar, M., Wang, Y., and He, J. (2014). Vertical SnSe nanorod arrays: from controlled synthesis and growth mechanism to thermistor and photoresistor. Nanotechnology *25*, 105705.

Carbone, I., Zhou, Q., Vollbrecht, B., Yang, L., Medling, S., Bezryadina, A., Bridges, F., Alers, G.B., Norman, J.T., and Kinmen, T. (2011). Pulsed chemical vapor deposition of Cu_2S into a porous TiO_2 matrix. J. Vac. Sci. Technol. A *29*, 051505.

Chang, Y., Cheng, Y., Feng, Y., Jian, H., Wang, L., Ma, X., Li, X., and Zhang, H. (2018). Resonance energy transfer-promoted photothermal and photodynamic performance of gold-copper sulfide yolk-shell nanoparticles for chemophototherapy of cancer. Nano Lett. *18*, 886–897.

Comin, A., and Manna, L. (2014). New materials for tunable plasmonic colloidal nanocrystals. Chem. Soc. Rev. *43*, 3957–3975.

Conley, B.R., Mosleh, A., Ghetmiri, S.A., Du, W., Soref, R.A., Sun, G., Margetis, J., Tolle, J., Naseem, H.A., and Yu, S.-Q. (2014). Temperature dependent spectral response and detectivity of GeSn photoconductors on silicon for short wave infrared detection. Opt. Express *22*, 15639–15652.

Cui, J., Li, Y., Liu, L., Chen, L., Xu, J., Ma, J., Fang, G., Zhu, E., Wu, H., Zhao, L., et al. (2015). Near-infrared plasmonic-enhanced solar energy harvest for highly efficient photocatalytic reactions. Nano Lett. *15*, 6295–6301.

Cui, Y., Wei, C., Yang, J., Zhang, J., and Zheng, W. (2016). Ionic liquid-assisted solvothermal synthesis of three-dimensional hierarchical copper sulfide microflowers at a low temperature

with enhanced photocatalytic performance. CrystEngComm *18*, 6245–6253.

Deng, K., and Li, L. (2014). CdS nanoscale photodetectors. Adv. Mater. *26*, 2619–2635.

Deng, X., Li, K., Cai, X., Liu, B., Wei, Y., Deng, K., Xie, Z., Wu, Z., Ma, P.a., Hou, Z., et al. (2017). A hollow-structured $CuS@Cu_2S@Au$ nanohybrid: synergistically enhanced photothermal efficiency and photoswitchable targeting effect for cancer theranostics. Adv. Mater. *29*, 1701266.

Ding, X., Liow, C.H., Zhang, M., Huang, R., Li, C., Shen, H., Liu, M., Zou, Y., Gao, N., Zhang, Z., et al. (2014). Surface plasmon resonance enhanced light absorption and photothermal therapy in the second near-infrared window. J. Am. Chem. Soc. *136*, 15684–15693.

Gao, W., Sun, Y., Cai, M., Zhao, Y., Cao, W., Liu, Z., Cui, G., and Tang, B. (2018). Copper sulfide nanoparticles as a photothermal switch for TRPV1 signaling to attenuate atherosclerosis. Nat. Commun. *9*, 231.

Habashi, F., and Dugdale, R. (1973). The reduction of sulfide minerals by hydrogen in the presence of lime. Metall. Trans. *4*, 1865–1871.

Han, S.-K., Gu, C., Zhao, S., Xu, S., Gong, M., Li, Z., and Yu, S.-H. (2016). Precursor triggering synthesis of self-coupled sulfide polymorphs with enhanced photoelectrochemical properties. J. Am. Chem. Soc. *138*, 12913–12919.

Herman, A., Vandenbem, C., Deparis, O., Simonis, P., and Vigneron, J.P. (2011). Nanoarchitecture in the Black Wings of Troides Magellanus: A Natural Case of Absorption Enhancement in Photonic Materials (SPIE NanoScience Engineering (International Society for Optics and Photonics), 80940H-80912.

Jia, Y., Yang, L., Xue, J., Zhang, N., Fan, D., Ma, H., Ren, X., Hu, L., and Wei, Q. (2019). Bioactivity-protected electrochemiluminescence biosensor using gold nanoclusters as the low-potential luminophor and Cu_2S snowflake as Co-reaction accelerator for procalcitonin analysis. ACS Sens. *4*, 1909–1916.

Jiang, Y., Yu, B.-B., Liu, J., Li, Z.-H., Sun, J.-K., Zhong, X.-H., Hu, J.-S., Song, W.-G., and Wan, L.-J. (2015). Boosting the open circuit voltage and fill factor of QDSSCs using hierarchically assembled $ITO@Cu_2S$ nanowire array counter electrodes. Nano Lett. *15*, 3088–3095.

Jiang, K., Liu, B., Luo, M., Ning, S., Peng, M., Zhao, Y., Lu, Y.-R., Chan, T.-S., de Groot, F.M.F., and Tan, Y. (2019). Single platinum atoms embedded in nanoporous cobalt selenide as electrocatalyst for accelerating hydrogen evolution reaction. Nat. Commun. *10*, 1743.

Johari, P., and Shenoy, V.B. (2011). Tunable dielectric properties of transition metal dichalcogenides. ACS Nano *5*, 5903–5908.

Jones, J., Xiong, H., DeLaRiva, A.T., Peterson, E.J., Pham, H., Challa, S.R., Qi, G., Oh, S., Wiebenga, M.H., Pereira Hernández, X.I., et al. (2016). Thermally stable single-atom platinum-on-ceria catalysts via atom trapping. Science *353*, 150.

Joo, J., Kim, T., Lee, J., Choi, S.-I., and Lee, K. (2019). Morphology-controlled metal sulfides and phosphides for electrochemical water splitting. Adv. Mater. *31*, 1806682.

Knight, M.W., Sobhani, H., Nordlander, P., and Halas, N.J. (2011). Photodetection with active optical antennas. Science *332*, 702.

Koppens, F.H.L., Mueller, T., Avouris, P., Ferrari, A.C., Vitiello, M.S., and Polini, M. (2014). Photodetectors based on graphene, other two-dimensional materials and hybrid systems. Nat. Nanotech. *9*, 780.

Kriegel, I., Rodríguez-Fernández, J., Como, E.D., Lutich, A.A., Szeifert, J.M., and Feldmann, J. (2011). Tuning the light absorption of $Cu_{1.97}S$ nanocrystals in supercrystal structures. Chem. Mater. *23*, 1830–1834.

Kriegel, I., Jiang, C., Rodríguez-Fernández, J., Schaller, R.D., Talapin, D.V., da Como, E., and Feldmann, J. (2012). Tuning the excitonic and plasmonic properties of copper chalcogenide nanocrystals. J. Am. Chem. Soc. *134*, 1583–1590.

Liu, X., Mayer, M.T., and Wang, D. (2010). Understanding ionic vacancy diffusion growth of cuprous sulfide nanowires. Angew.Chem. Int. Ed. *49*, 3165–3168.

Liu, Y., Deng, Y., Sun, Z., Wei, J., Zheng, G., Asiri, A.M., Khan, S.B., Rahman, M.M., and Zhao, D. (2013). Hierarchical Cu_2S microsponges constructed from nanosheets for efficient photocatalysis. Small *9*, 2702–2708.

Liu, P.-H., Lin, C.-C., Manekkathodi, A., and Chen, L.-J. (2015). Multilevel resistance switching of individual Cu_2S nanowires with inert electrodes. Nano Energ. *15*, 362–368.

Liu, S., Tian, J., Wu, S., Jia, X., Luo, M., and Zhang, W. (2020). A flower-inspired divergent light-trapping structure with quasi-spherical symmetry towards a high-performance flexible photodetector. Nanoscale 12, 20898.

Lopez-Sanchez, O., Lembke, D., Kayci, M., Radenovic, A., and Kis, A. (2013). Ultrasensitive photodetectors based on monolayer MoS_2. Nat. Nanotech. 8, 497.

Luther, J.M., Jain, P.K., Ewers, T., and Alivisatos, A.P. (2011). Localized surface plasmon resonances arising from free carriers in doped quantum dots. Nat. Mater. 10, 361–366.

Manzi, A., Simon, T., Sonnleitner, C., Döblinger, M., Wyrwich, R., Stern, O., Stolarczyk, J.K., and Feldmann, J. (2015). Light-induced cation exchange for copper sulfide based CO_2 reduction. J. Am. Chem. Soc. 137, 14007–14010.

Martinson, A.B.F., Riha, S.C., Thimsen, E., Elam, J.W., and Pellin, M.J. (2013). Structural, optical, and electronic stability of copper sulfide thin films grown by atomic layer deposition. Energy Environ. Sci. 6, 1868–1878.

Pan, C., Niu, S., Ding, Y., Dong, L., Yu, R., Liu, Y., Zhu, G., and Wang, Z.L. (2012). Enhanced Cu_2S/ CdS coaxial nanowire solar cells by piezo-phototronic effect. Nano Lett. 12, 3302–3307.

Qiao, B., Wang, A., Yang, X., Allard, L.F., Jiang, Z., Cui, Y., Liu, J., Li, J., and Zhang, T. (2011). Single-atom catalysis of CO oxidation using Pt1/FeOx. Nat. Chem. 3, 634–641.

Ren, K., Yin, P., Zhou, Y., Cao, X., Dong, C., Cui, L., Liu, H., and Du, X. (2017). Localized defects on copper sulfide surface for enhanced plasmon resonance and water splitting. Small 13, 1700867.

Riha, S.C., Johnson, D.C., and Prieto, A.L. (2011). Cu_2Se nanoparticles with tunable electronic properties due to a controlled solid-state phase transition driven by copper oxidation and cationic conduction. J. Am. Chem. Soc. 133, 1383–1390.

Saran, R., and Curry, R.J. (2016). Lead sulphide nanocrystal photodetector technologies. Nat. Photon. 10, 81–92.

Saranya, M., Ramachandran, R., Samuel, E.J.J., Jeong, S.K., and Grace, A.N. (2015). Enhanced visible light photocatalytic reduction of organic pollutant and electrochemical properties of CuS catalyst. Powder Technol. 279, 209–220.

Scotognella, F., Della Valle, G., Srimath Kandada, A.R., Dorfs, D., Zavelani-Rossi, M., Conforti, M., Miszta, K., Comin, A., Korobchevskaya, K., Lanzani, G., et al. (2011). Plasmon dynamics in colloidal $Cu_{2-x}Se$ nanocrystals. Nano Lett. 11, 4711–4717.

Tagirov, B.R., Dikov, Y.P., Buleev, M.I., Koval'chuk, E.V., Chareev, D.A., Kokh, M.A., Borisovskii, S.E., Abramova, V.D., Baranova, N.N., Garas'ko, M.I., et al. (2014). "Invisible" gold in covellite (CuS): synthesis and studies by EPMA, LA-ICP-MS, and XPS techniques. Dokl. Earth Sci. 459, 1381–1386.

Tagirov, B.R., Trigub, A.L., Kvashnina, K.O., Shiryaev, A.A., Chareev, D.A., Nickolsky, M.S., Abramova, V.D., and Kovalchuk, E.V. (2016). Covellite CuS as a matrix for "invisible" gold: X-ray spectroscopic study of the chemical state of Cu and Au in synthetic minerals. Geochim.Cosmochim. Acta 191, 58–69.

Tian, Q., Tang, M., Sun, Y., Zou, R., Chen, Z., Zhu, M., Yang, S., Wang, J., Wang, J., and Hu, J. (2011). Hydrophilic flower-like CuS superstructures as an efficient 980 nm laser-driven photothermal agent for ablation of cancer cells. Adv. Mater. 23, 3542–3547.

Tian, J., Zhang, W., Gu, J., Deng, T., and Zhang, D. (2015a). Bioinspired Au-CuS coupled photothermal materials: enhanced infrared absorption and photothermal conversion from butterfly wings. Nano Energ. 17, 52–62.

Tian, J., Zhang, W., Huang, Y., Liu, Q., Wang, Y., Zhang, Z., and Zhang, D. (2015b). Infrared-induced variation of the magnetic properties of a magnetoplasmonic film with a 3D sub-micron periodic triangular roof-type antireflection structure. Sci. Rep. 5, 8025.

Tian, J., Zhang, W., Fang, X., Liu, Q., Gu, J., Deng, T., Wang, Y., and Zhang, D. (2015c). Coupling of plasmon and 3D antireflection quasi-photonic crystal structure for enhancement infrared absorption. J. Mater. Chem. C 3, 1672–1679.

Tian, J., Wen, Y., Wang, Y., Jia, X., Chen, L., Qiao, R., Zhang, W., Zhang, D., and Zhong, J. (2019). Mapping thermal radiation in plasmonic structures. Chem. Phys. 526, 110423.

Tian, J., Chen, L., Qiao, R., Xiong, K., Zhang, W., Mao, Y., Li, H., and Li, J. (2021). Photothermal-assist enhanced high-performance self-powered photodetector with bioinspired temperature-autoregulation by passive radiative balance. Nano Energ. 79, 105435.

Wang, W., Zhang, W., Fang, X., Huang, Y., Liu, Q., Bai, M., and Zhang, D. (2014). Omnidirectional light absorption of disordered nano-hole structure inspired from Papilio ulysses. Opt. Lett. 39, 4208–4211.

Wang, X., Ke, Y., Pan, H., Ma, K., Xiao, Q., Yin, D., Wu, G., and Swihart, M.T. (2015). Cu-deficient plasmonic $Cu_{2-x}S$ nanoplate electrocatalysts for oxygen reduction. ACS Catal. 5, 2534–2540.

Wei, H., Liu, X., Wang, A., Zhang, L., Qiao, B., Yang, X., Huang, Y., Miao, S., Liu, J., and Zhang, T. (2014). FeOx-supported platinum single-atom and pseudo-single-atom catalysts for chemoselective hydrogenation of functionalized nitroarenes. Nat. Commun. 5, 5634.

Wong, A.B., Brittman, S., Yu, Y., Dasgupta, N.P., and Yang, P. (2015). Core-Shell CdS-Cu_2S nanorod array solar cells. Nano Lett. 15, 4096–4101.

Wu, Y., Wadia, C., Ma, W., Sadtler, B., and Alivisatos, A.P. (2008). Synthesis and photovoltaic application of copper(I) sulfide nanocrystals. Nano Lett. 8, 2551–2555.

Wu, X., Robson, M.E., Phelps, J.L., Tan, J.S., Shao, B., Owens, G., and Xu, H. (2019). A flexible photothermal cotton-CuS nanocage-agarose aerogel towards portable solar steam generation. Nano Energ. 56, 708–715.

Xie, Y., Zhang, B., Wang, S., Wang, D., Wang, A., Wang, Z., Yu, H., Zhang, H., Chen, Y., Zhao, M., et al. (2017). Ultrabroadband MoS_2 photodetector with spectral response from 445 to 2717 nm. Adv. Mater. 29, 1605972.

Xu, Q., Huang, B., Zhao, Y., Yan, Y., Noufi, R., and Wei, S.-H. (2012). Crystal and electronic structures of Cu_xS solar cell absorbers. Appl. Phys. Lett. 100, 061906.

Yang, X.-F., Wang, A., Qiao, B., Li, J., Liu, J., and Zhang, T. (2013). Single-atom catalysts: a new frontier in heterogeneous catalysis. Acc. Chem. Res. 46, 1740–1748.

Yao, H.-B., Fang, H.-Y., Wang, X.-H., and Yu, S.-H. (2011). Hierarchical assembly of micro-/nano-building blocks: bio-inspired rigid structural functional materials. Chem. Soc. Rev. 40, 3764–3785.

Youngblood, N., Chen, C., Koester, S.J., and Li, M. (2015). Waveguide-integrated black phosphorus photodetector with high responsivity and low dark current. Nat. Photon. 9, 247.

Yu, K., Fan, T., Lou, S., and Zhang, D. (2013a). Biomimetic optical materials: integration of nature's design for manipulation of light. Prog.Mater. Sci. 58, 825–873.

Yu, W.J., Liu, Y., Zhou, H., Yin, A., Li, Z., Huang, Y., and Duan, X. (2013b). Highly efficient gate-tunable photocurrent generation in vertical heterostructures of layered materials. Nat. Nanotech. 8, 952.

Yu, Y.-X., Pan, L., Son, M.-K., Mayer, M.T., Zhang, W.-D., Hagfeldt, A., Luo, J., and Grätzel, M. (2018). Solution-processed Cu_2S photocathodes for photoelectrochemical water splitting. ACS Energ. Lett. 3, 760–766.

Zhang, D., Zhang, W., Gu, J., Fan, T., Liu, Q., Su, H., and Zhu, S. (2015). Inspiration from butterfly and moth wing scales: characterization, modeling, and fabrication. Prog.Mater. Sci. 68, 67–96.

Zhao, Q., Guo, X., Fan, T., Ding, J., Zhang, D., and Guo, Q. (2011). Art of blackness in butterfly wings as natural solar collector. Soft Matter 7, 11433–11439.

Zhuang, T.-T., Liu, Y., Li, Y., Zhao, Y., Wu, L., Jiang, J., and Yu, S.-H. (2016). Integration of semiconducting sulfides for full-spectrum solar energy absorption and efficient charge separation. Angew.Chem. Int. Ed. 55, 6396–6400.

Supplemental information

A bioinspired Au-Cu$_{1.97}$S/Cu$_2$S film

with efficient low-angle-dependent

and thermal-assisted photodetection properties

Junlong Tian, Ruyi Qiao, Kai Xiong, Wang Zhang, and Lulu Chen

Supplemental Information
Transparent Methods

A bioinspired Au-Cu$_{1.97}$S/Cu$_2$S film with efficient low-angle-dependent and thermal-assisted photodetection properties

Junlong Tian,[1*‡] Ruyi Qiao,[1‡] Kai Xiong,[2] Wang Zhang,[3*] and Lulu Chen[1]

[1] Hunan Key Laboratory of Micro-Nano Energy Materials and Devices, Laboratory for Quantum Engineering and Micro-Nano Energy Technology, School of Physics and Optoelectronic, Xiangtan University, Xiangtan, Hunan 411105, China.

[2] College of Materials Science and Engineering, Yunnan University, Kunming, Yunnan 650091, China.

[3] State Key Laboratory of Metal Matrix Composites, Shanghai Jiao Tong University, Shanghai 200240, China.

[*] Author to whom correspondence should be addressed: jltian666@xtu.edu.cn, wangzhang@sjtu.edu.cn.

[‡] Junlong Tian and Ruyi Qiao contributed equally to this work.

Experimental

Chemicals

Troides helena butterflies were obtained from Shanghai Natural Wild-Insect Kingdom Co., Ltdj. Ethanol absolute (EA, 99.7%). Nitric acid (NA, 67%), Ethylenediamine (ED, 99.9%) were purchased from Tian in Fuyu Fine Chemicals Co., Ltdj. Chloroauric acid tetrahydrate (HAuCl$_4$, 47.8%) was purchased from Sinopharm Chemical Reagent Co., Ltd., Sodium borohydride (NaBH$_4$, 98%) was purchased from XILONG SCIENTIFIC. Sodium chloride (NaCl, 99.5%) was purchased from TIANJIN YONGDA CHEMICAL REAGENT COMPANY LIMITED. Diethanolamine (DEA, 99%) was purchased from Tianjin Hengxing Chemical Preparation Co..Ltd. Copper (II) Chloride dehydrate (CuCl$_2$·2H$_2$O, 99%) was purchased from Tianjin Damao Chemicals Co., Ltdj., Ammonia solution (NH$_3$·H$_2$O, 26%) and Thiourea (99%) were purchased from XILONG SCIENTIFIC. All of these are analytically pure and were used as received without further purification.

Preparations of morph-genetic metal/semiconductor function material and photodetector

1. Synthesis of Au-T_FW

(1) Amination of biotemplate

The forewing of *Troideshelena* butterflies (T_FWs) were firstly immersed in the ethanol for 30 minutes to wash off the surface impurities and then rinsed with deionized water for several times. The T_FWs were immersed in diluted nitric acid (8 vol%) for 2 hours and used deionized water to remove residuals. The T_FWs were immersed in an ethanol solution of Ethylenediamine (25 vol%) for 6 hours to activate the T_FWs, and they were firstly washed with ethanol solution and then rinsed with deionized water (Tan et al., 2011).

(2) Nanoseed growth

The aminated wings were immerged in 0.2 weight percentage (wt%) $HAuCl_4$ solution prepared by dissolving $HAuCl_4$ into equal weights of ethanol and deionized water for 4 hours. After 4 hours, flushed out the remaining $HAuCl_4$ solution with deionized water, and immersed wings in a $NaBH_4$ (0.1 mol/L) aqueous solution for 2 minutes, and then rinsed with deionized water (Tan et al., 2011).

(3) Au deposition

The Au nanoseed functionalized butterfly wings were immersed in a specific electroless deposition solution for 4 hours. The electroless deposition solution was prepared by mixing solution A and B in equal volume (A: NaCl 2 g and $HAuCl_4$ 1 g dissolved in 100 mL deionized water; B: Diethanolamine (DEA) 2 g and ethanol 20 mL dissolved in 100 mL deionized water). Both A and B were prepared and stored in 4 ℃ for using (Wu et al., 2018).

2.Synthesis of Au-CuS-T_FW

The CuS nanoparticle synthesis solution was prepared by mixing 20 ml $CuCl_2 \cdot 2H_2O$ (0.4 mol/L), 40 ml $NH_3 \cdot H_2O$ and 20 ml Thiourea (1 mol/L) with magnetic stirring for 30 minutes. Then, the

Au-T_FWs were immersed in the CuS nanoparticle synthesis solution and sealed in an autoclave heated at 80 ℃ for 2 hours. After being cooled down to room temperature, the treated wings were taken out and washed with deionized water. Then, they were put in the vacuum of 60 ℃ for 12 hours for drying (Tian et al., 2015a).

3. Synthesis of Au-Cu$_{1.97}$S/Cu$_2$S-C-T_FW

The dried Au-CuS-T_FW is placed in the hot center of the tube furnace vented with 5:95 H$_2$/Ar mixture gases at 50 sccm. The center of the furnace is gradually heated from room temperature to 450 ℃ at a rate of 7.5 ℃/min, and then the chamber is maintained at 450 ℃ for 120 min. Meanwhile, the chitin-matrix template (T_FW) has been carbonized to enhance the IR absorption during this sintering process. Last, because the stoichiometric Cu$_2$S NPs are prone to oxidation into more thermodynamically stable and nonstoichiometric copper chalcogenide phases containing both Cu$^+$ and Cu^{2+} ions, when the Au-Cu$_2$S-C-T_FW film is exposed to air under ambient conditions, the Cu$_2$S NPs located at the surface of the Au-Cu$_2$S-C-T_FW film are transformed in the thermodynamically stable nonstoichiometric Cu$_{1.97}$S phase (Au-Cu$_{1.97}$S/Cu$_2$S-C-T_FW) spontaneously.

4. Fabrication of Au-Cu$_{1.97}$S/Cu$_2$S-C-T_FW(20 h)

The preparation of the Au-Cu$_{1.97}$S/Cu$_2$S-C-T_FW(20 h) is the same as Au-Cu$_{1.97}$S/Cu$_2$S-C-T_FW photodetector, where the difference is that the Au-T_FWs were immersed in the CuS nanoparticle synthesis solution and sealed in an autoclave heated at 80 ℃ for 20 hours.

5. Fabrication of Cu$_{1.97}$S/Cu$_2$S-C-T_FW

The preparation of the Cu$_{1.97}$S/Cu$_2$S-C-T_FW photodetector is the same as Au-Cu$_{1.97}$S/Cu$_2$S-C-T_FW photodetector, where the difference is that the Cu$_{1.97}$S/Cu$_2$S-C-T_FW photodetector lack the process of Au deposition.

6. Fabrication of photodetector

The fabricated devices with Ag paste as contacts whose effective area (S) is 0.5 mm^2 (0.5 mm × 1

mm) were utilized for broadband photodetector. Unless otherwise specified, the measurements were performed at room temperature. Here, the ambient temperature is 20 ℃.

Characterization

The morphology was examined with an extended depth-of field optical microscope (VHX-1000E, Keynce) and scanning Electron microscope (SEM, Quanta 250) equipped with an EDS (Oxford Instruments). Transmission electron microscope (TEM), high-resolution transmission electron microscope (HRTEM) and selected-area electron diffraction (SAED) measurements were performed on a JEM-2100F transmission Electron microscope (JEOL, Peabody). X-ray diffraction (XRD) Measurements conducted using */LXRD produced by Proto, Canada. X-ray photoelectron spectroscopy (XPS) was carried out using Thermo SCIENTIFIC K-ALPHA. The absorption over the wavelength range of 300-2500 nm was measured using a Lambda 750 UV-vis-NIR spectrophotometer (PerkinElmer, Waltham, MA, USA). The absorption over the wavelength range of 400-810 nm were measured using an angle-resolved spectrum system in micro-region (ARM, ideaoptics, China). The infrared absorption over the wavelength range of 2.5-25 μm was measured by a Nicolet 6700 Fourier Transform infrared spectrometer. PL spectra were collected by using Laser emission steady-state spectrometer, excited at room temperature with excitation laser wavelength of 532 nm.

Electric and photoresponse measurements

Electric and Photoresponse measurements were measured on Keithley 2400 Test System. The bias potential of the photodetector was measured at 0.5 V. The wavelengths of the excitation laser were 660 nm, 808 nm and 980 nm, respectively. The effective area is 0.5 mm^2.The intensities of the excitation laser were 0.06mWmm^{-2}, 0.11mW mm^{-2}, 0.56mW mm^{-2}, 1.11mW mm^{-2}, 1.67mW mm^{-2}, respectively. The stability of the photodetector was all measured under1.67mW mm^{-2} at 0.5 V bias potential. All these operations were excited and measured at room temperature (20 ℃).

Heat measurements

The heat was reflected by temperature in this experiment. The temperature of the photodetector was measured by a paperless recorder (YT-2-No.12180042), which was purchased from Yateks$^{®}$. The

photodetector was pasted by aluminum foil with thermal grease. The probe of the recorder was put under the aluminum foil to monitor the temperature.

The heat source was added by a precision adjustable DC regulated power supply (HSPY-36-03). The poser source could be connected to a ceramic heating sheet to provide the additional temperature. The photodetector was also bonded with the ceramic heating sheets by using thermal grease.

Simulation

1. Modeling and FDTD simulation

An FDTD simulation is adopted to simulate the optical absorption, Poynting vector intensity distribution maps and $|\vec{E}|^2$ intensity distribution maps. As shown in Figure S7, the models for FDTD simulation of Cu$_2$S_NPs (a single layer of Cu$_2$S nanosphere array), C-T_FW and Cu$_2$S-C-T_FW (adding two layers of the Cu$_2$S nanospheres array to the surface of C-T_FW) are built on the basis of the SEM and TEM of the T_FW (Figure S1) and Au-Cu$_{1.97}$S/Cu$_2$S-C-T_FW (Figure 2c-f and S4). The detailed structural dimensions are shown in Table S1. For the FDTD simulation model of the Cu$_2$S-C-T_FW, two Cu$_2$S_NPs layers covered the surface of the T_FW. Figure S7 are the FDTD simulation models for a single layer of the Cu$_2$S nanosphere array (CuS_NPs), C-T_FW and Cu$_2$S-C-T_FW (adding two layers of the Cu$_2$S nanospheres array to the surface of C-T_FW), respectively. The diameter of Cu$_2$S nanosphere is 20 nm (Figure S4). All FDTD simulations are performed under normal incident light with a plane wave light source. The wavelength is fixed under 300-2500 nm. The light source is laid above the simulation model at a distance of 500 nm. The boundary condition in the y direction is periodic (periodic boundary condition, PBC), and in the z direction is absorbing (perfectly matched layer, PML). The span of the x direction is zero. Here in our simulation, the complex permittivity index of the Cu$_2$S and amorphous carbon (450 ℃) are provided by the material database of the Optiwave and the reported results(Smith, 1984; Gao and Jiang, 2004),respectively. The observation plane for transmission (T) was located 100 nm beneath the model, and the observation plane for reflection (R) was 500 nm from the top of the light source. The calculation formula for absorption is as follows: A=1-T-R. The mesh size was chosen to obtain a good tradeoff between the computer memory required and the simulation time, while ensuring convergence of the results. A convergence test was carefully performed.

2. Calculation of the photothermal conversion

The absorbed photons cause transitions from a lower energy set of quantum states (*L*), which is generally composed of the substrates of the ground electronic states of the absorbing centers, to an upper set of states (*U*), which is composed of the excited electronic states of the absorbing centers. The potential difference between the band is

$$\Delta p = \Delta E - T\Delta S \qquad (1)$$

where $\Delta E = h\nu$ is the energy for absorbing a photon. *T* is the ambient temperature, and ΔS is the entropy change per absorbed photon. The hot power yield will be

$$H = \Delta p_{use} \cdot n_{absorbed} \qquad (2)$$

where $n_{absorbed}$ is the number of photon absorption. Δp_{use} is the from Eq. (1) as carriers from one absorbed photon traverse a utilization pathway removing energy from the absorber. Consequently, the intensive electromagnetic field energy flux density regions located on the surface of the ridges of the Cu₂S-C-T_FW correspond to more photon distribution regions, which promote photon absorption and advance the yielding of more hot power.

When a plasmonic structure is under illumination, the heat source density arises from the Joule effect (Hao and Schatz, 2004; Baffou et al., 2010):

$$h(\vec{r}) = \frac{1}{2}[j^*(\vec{r}) \cdot E(\vec{r}) + j(\vec{r}) \cdot E^*(\vec{r})] \qquad (3)$$

where $j(\vec{r})$ and $E(\vec{r})$ are the complex amplitudes of the electronic current density and the electric field, respectively. The relation enables us to express the heat source density as a function of the electric field from Eq. (3):

$$h(\vec{r}) = \omega\varepsilon_0 lm(\varepsilon_\omega)|E(\vec{r})|^2 \qquad (4)$$

where ω is the angular frequency of the light and ε_ω is the permittivity of the material. The temperature $T(\vec{r})$ is given by a linear super position:

$$T(\vec{r}) = \sum_{j=1}^{N} G(\vec{r},\vec{r_j}) \cdot h(\vec{r}) \qquad (5)$$

where $G(\vec{r},\vec{r_j})$ is the Green's function associated with the system (Baffou et al., 2010). In the Green's function, the thermal conductivities of air and Cu₂S are 0.025 W/m K (Baffou et al., 2010) and 0.32 W/m K (Gao and Jiang, 2004), respectively.

3. Calculation details of the thermal radiation

Kirchhoff's law states that for an object in thermal equilibrium with the surrounding radiation field, its absorptivity and emissivity are equal, for every frequency, direction and polarization. In this work, The thermal radiation spectrum (*Thermal_radiation(λ,T)*) is calculated on the basis of the Kirchhoff's law:

$$Thermal\_radiation(λ,T)=A(λ) \qquad\qquad (6)$$

where *A(λ)* is the absorbance spectrum.

4. Mapping the thermal radiation in plasmonic structures

In order to map the thermal radiation in the plasmonic structures, frist of all, we use the FDTD method to calculate the $|E(\vec{r}, \lambda_i)|^2$ at a related wavelength (λ_i). Then, the heat source density $(h(\vec{r}, \lambda_i))$ which resulted from photothermal conversion irradiated by a related wavelength (λ_i) is calculated by means of Equation (4). Following, the temperature $(T(\vec{r}, \lambda_i))$ which resulted from photothermal conversion irradiated by a related wavelength (λ_i) is calculated via Equation (5). Lastly, the blackbody radiation maps are simulated by substituting $T(\vec{r}, \lambda_i)$ into the Planck's Blackbody radiation formula and rearranging to get:

$$M_{B\lambda}\left(\lambda_i, T(\vec{r}, \lambda_i)\right) = 2\pi hc^2 \lambda_i^{-5} \frac{1}{\frac{hc}{(e^{\lambda_i kT(\vec{r},\lambda_i)}-1)}} \qquad\qquad (7)$$

Reasonably, the intensive electromagnetic field energy flux density regions correspond to more photon distribution regions, which promote photon absorption and advance the yielding of more hot power. Moreover, the imaginary part of the complex index of refraction name extinction coefficient related to the optical absorption of the material. Consequently, combined the relationship between the optical absorption of the material and the electromagnetic field energy flux density as well as the imaginary part of the complex index of refraction, in this work, the absorption per unit volume is calculated as a function of space and wavelength:

$$A(\vec{r}, \lambda_i) = 0.5\omega \left|\vec{E}(\vec{r}, \lambda_i)\right|^2 imag(\varepsilon(\vec{r}, \lambda_i)) \qquad\qquad (8)$$

where ω is circular frequency, $imag(\varepsilon(\vec{r}, \lambda_i))$ is the imaginary part of the complex permittivity. On

the basis of the Kirchhoff's law and Planck's Blackbody radiation law, the thermal radiation is mapped by multiplying the absorbance spectrum by blackbody radiation spectrum:

$$Thermal\_radiation(\lambda, h)_{\lambda_i} = A(\vec{r}, \lambda_i) * M_{B\lambda}(\lambda_i, T(\vec{r}, \lambda_i)) \quad (9)$$

more detailedly expressed as:

$$Thermal\_radiation(\lambda, h)_{\lambda_i} = \left\{ 0.5\omega |\vec{E}(\vec{r}, \lambda_i)|^2 imag(\varepsilon(\vec{r}, \lambda_i)) \right\} * \left\{ 2\pi h c^2 \lambda_i^{-5} \frac{1}{(e^{\frac{hc}{\lambda_i kT(\vec{r}, \lambda_i)}} - 1)} \right\} \quad (10)$$

5. Density function theory (DFT) calculations

All DFT calculations performed using projector augmented wave (PAW), along with Vienna Abinitio Simulation Package (VASP) (Hafner,

2008). Meanwhile, The Perdew-Burke-Ernzerhof (PBE)(Atwater and Polman,

2010) form of the Gene-ralized-Gradient Approximation (GGA) (Itoh et al.,

2017) is used to describe the exchange and correlation functional.

The DFT-D3 empirical correction method was employed to accurately describe the van der Waals interactions(Dion et al., 2004). To investigate the Au-Cu-S solid solution system, we calculated the electronic properties of Cu_2S nanoparticle and Cu_2S nanoparticle doped with one Au atom, including the deformation charge density, energy band structure and density of states, respectively. The structure of Cu_2S nanoparticle was quoted from the research of professor Su-Huai Wei，provided by doctor Qiang Xu (Xu et al., 2012).
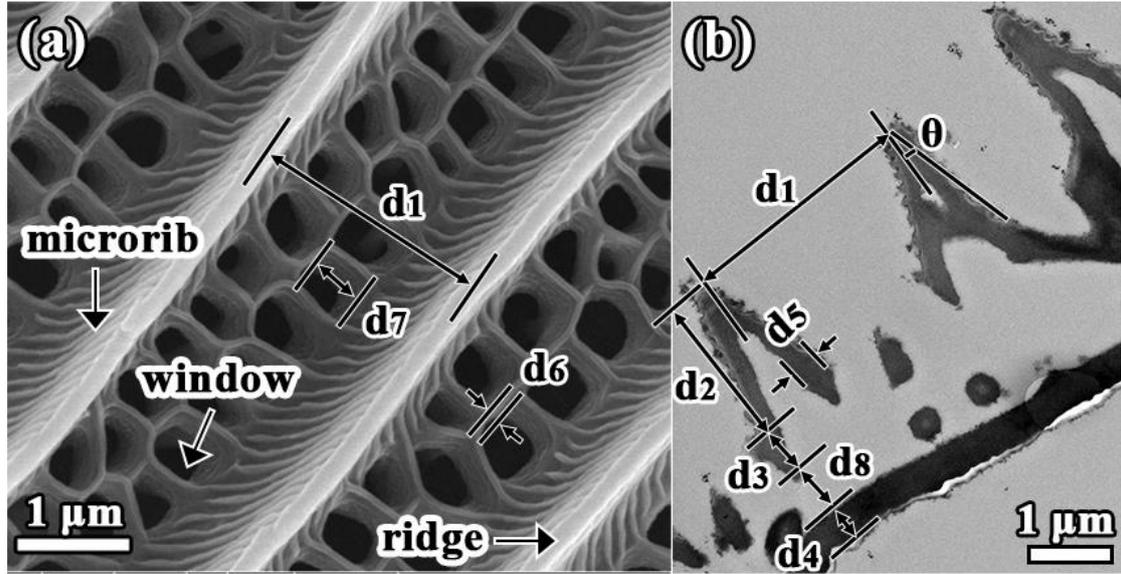
Figure S1. (a) SEM and (b) cross-section TEM images of T_FW. Related to Figure 2.

Table S1. Dimensions of the scale of the *T.helena* forewing. Related to Figure 2 and Figure S1.

	Value
d1: the period of the ridge-spacer structure (μm)	2.890
d2: the height of the ridges (μm)	2.238
d3: the depth of the window (μm)	0.658
d4: the thickness of the base slab (μm)	0.368
d5: the thickness of the ridge wall (μm)	0.236
d6: the thickness of the window well (μm)	0.180
d7: the width of the window (μm)	0.534
d8: the distance between the bottom of the window and the base slab (μm)	0.526
θ: the half vertex angle of the ridge (°)	13.0

As shown in Figure S1, the quasi-periodic triangular roof-type ridges run the length of the scale, and they can focus light into the scale interior via multiple antireflections. Double-row-staggered quasi-periodic lattice works are present between every two ridges, forming a series of windows that elongate the effective light path and the energy density distribution interspace. In addition, declining micro-ribs run down the sides of the ridge, and they induce internal light scattering and assist in trapping light. The dimensions (d1-d8 and θ, as shown in Figure S1) for the architecture of each element range from 2900 to 180 nm which are obtained by statistical analysis of several images obtained from the SEM and TEM, as listed in Table S1. Thus, the combined broad-scale distribution (2900-100 nm), antireflection ridges, declining micro-ribs and windows construct a hierarchical antireflection light absorption micro/nano-structure (HASAS) with excellent broadband light harvesting from the visible (VIS) to near infrared (NIR) regions (300-2500 nm), as shown in Figure 1a (Tian et al., 2015a; Tian et al., 2015b; Zhao et al., 2011).
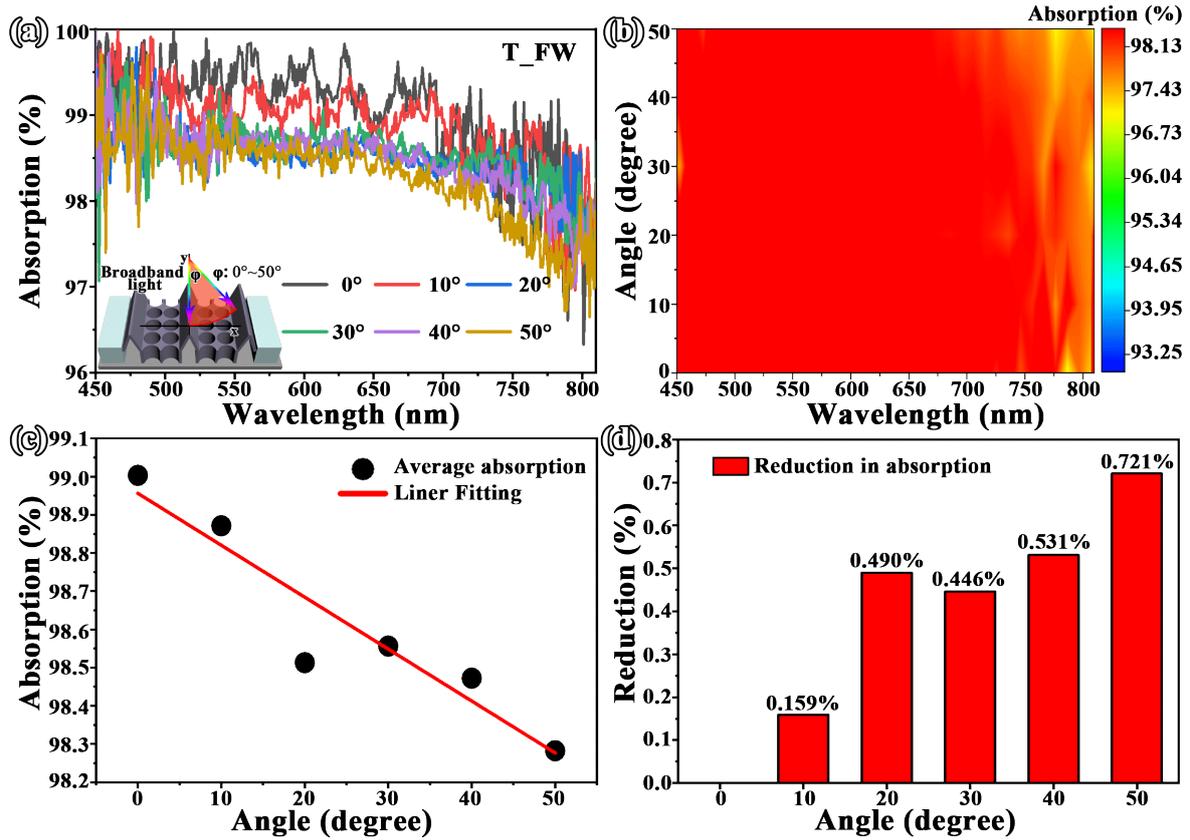
Figure S2. (a) The absorption spectra of T_FW at angles of 0°, 10°, 20°, 30°, 40° and 50° over the wavelength range from 450 nm to 810 nm, insert is the schematic illustration of incident at different angles of the photodetector. (b) Filled contour plot of angular dependence versus wavelength. (c) The average absorption of T_FW and the linear fitting of the average absorption. (d) Column chart of the reduction in absorption of T_FW. Related to Figure 3.

Moreover, the nano-hole window structures combined with the antireflection triangular roof-type ridges produce omnidirectional light absorption.(Wang et al., 2014) In Figure S2, the T_FW exhibits super low-angle-dependent light absorption over the VIS band (450-810 nm) (Figure S2a and b). When the incidence angle is up to 50°, the average light absorbance is still up to 98.3% (Figure S2c), and the reduction rate of absorptivity of T_FW is only 0.721% (Figure S2d) compared with the normal incidence.
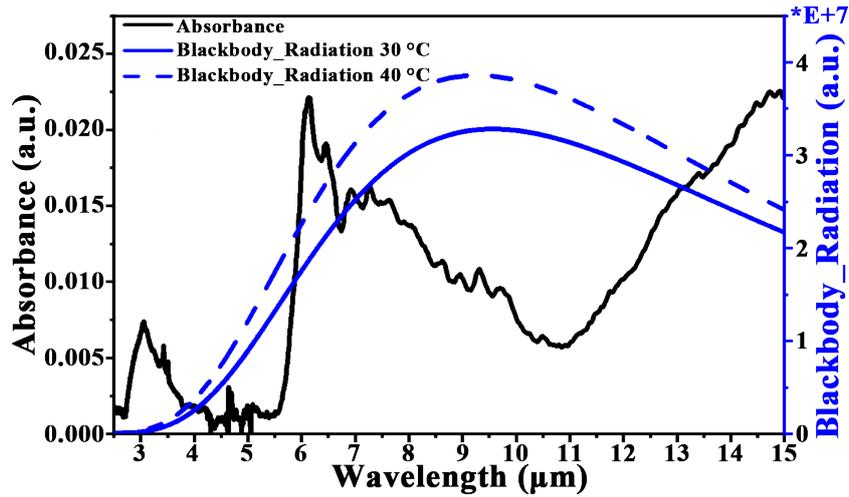
Figure S3. The absorbance of T_FW and blackbody radiation at temperature of 30 ℃ and 40 ℃ over the wavelength range from 2.5 μm to 15 μm. Related to Figure 3.

Naturally, the T_FW reveals several strong peaks of absorbance at 6.15, 6.48 and 7.27 μm (Figure S3), which predicts the spectral emissivity of T_FW because Kirchhoff's law states that the emission is equal to the absorption (Arpin et al., 2013). Due to the overlap of the thermal radiation peaks (centered on 6.15, 6.48 and 7.27 μm) with blackbody radiation at 40 ℃, the emissivity stays at a relatively constant value up to 40 ℃ and increases beyond this value. In particular, the thermal radiation peaks centered on 6.15 and 6.48 μm are positioned on the edge of the blackbody radiation for 40 ℃, and it plays a key role as the thermal regulator (Berthier, 2005; Herman et al., 2011). Accordingly, the radiation regulation plays a key role as a thermal regulator which modulates the energetic balance to prevent overheating and provides temperature auto-regulation.

Therefore, T_FW with HASAS have both good absorption (omnidirectional and broadband absorption) and effective emissivity to achieve temperature auto-regulation (Herman et al., 2011).
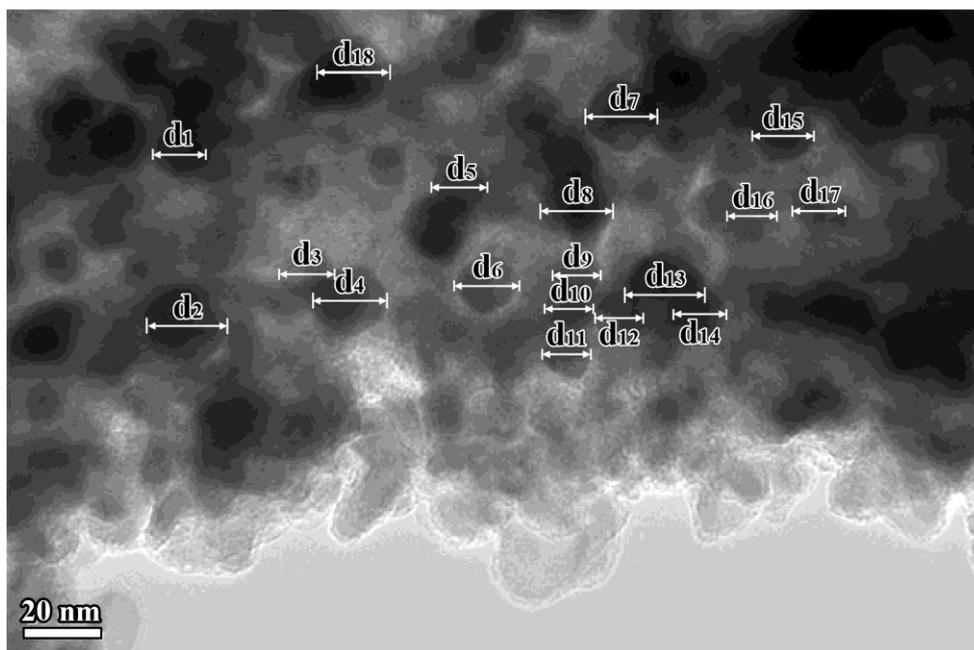
Figure S4. Diameter measurement of Au-Cu$_{1.97}$S/Cu$_2$S nanoparticles. Related to Figure 2.

Table S2. Diameter measurement of Au-Cu$_{1.97}$S/Cu$_2$S nanoparticles. Related to Figure 2 and Figure S4.

	Value (nm)		**Value (nm)**
d1	13.551	**d10**	12.336
d2	20.467	**d11**	12.336
d3	14.299	**d12**	12.336
d4	18.972	**d13**	20.561
d5	14.393	**d14**	13.645
d6	16.822	**d15**	15.794
d7	18.505	**d16**	12.804
d8	18.598	**d17**	13.645
d9	12.336	**d18**	18.667
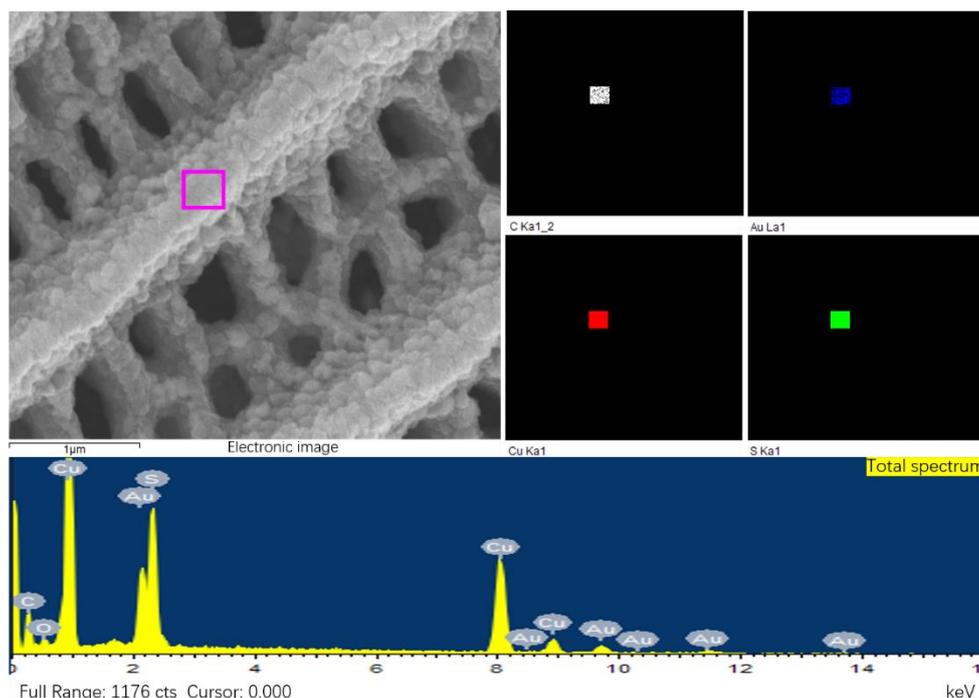
Figure S5. Electron energy loss spectroscopy analysis of Au-Cu$_{1.97}$S/Cu$_2$S-C-T_FW. Related to Figure 2.
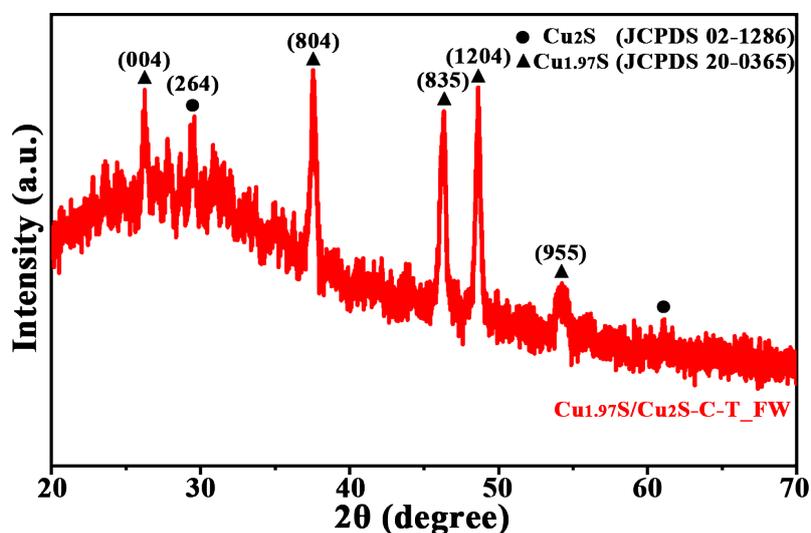
Figure S6. XRD result of Cu$_{1.97}$S/Cu$_2$S-C-T_FW. Related to Figure 2.

Additionally, according to the XRD pattern of Cu$_{1.97}$S/Cu$_2$S-C-T_FW (Figure S6), we can also conclude that the Cu$_2$S NPs located at the surface of Cu$_2$S-C-T_FW is transformed during the thermodynamically stable nonstoichiometric Cu$_{1.97}$S phase and forms a protective layer for stabilizing the Cu$_{1.97}$S/Cu$_2$S-C-T_FW.
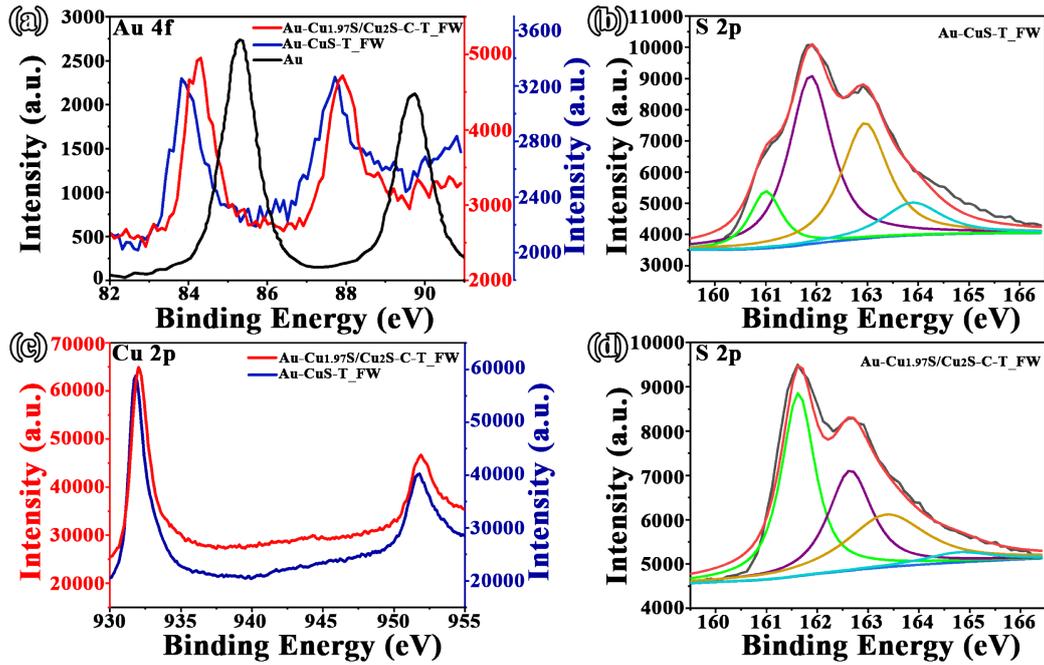
Figure S7. XPS spetra of (a) Au 4*f* for pure Au(Ding et al., 2014), Au-CuS-T_FW and Au-Cu$_{1.97}$S/Cu$_2$S-C-T_FW; (b) S 2*p* for Au-CuS-T_FW; (c) Cu2*p* for Au-CuS-T_FW and Au-Cu$_{1.97}$S/Cu$_2$S-C-T_FW; (d) S 2*p* for Au-Cu$_{1.97}$S/Cu$_2$S-C-T_FW. Related to Figure 2.
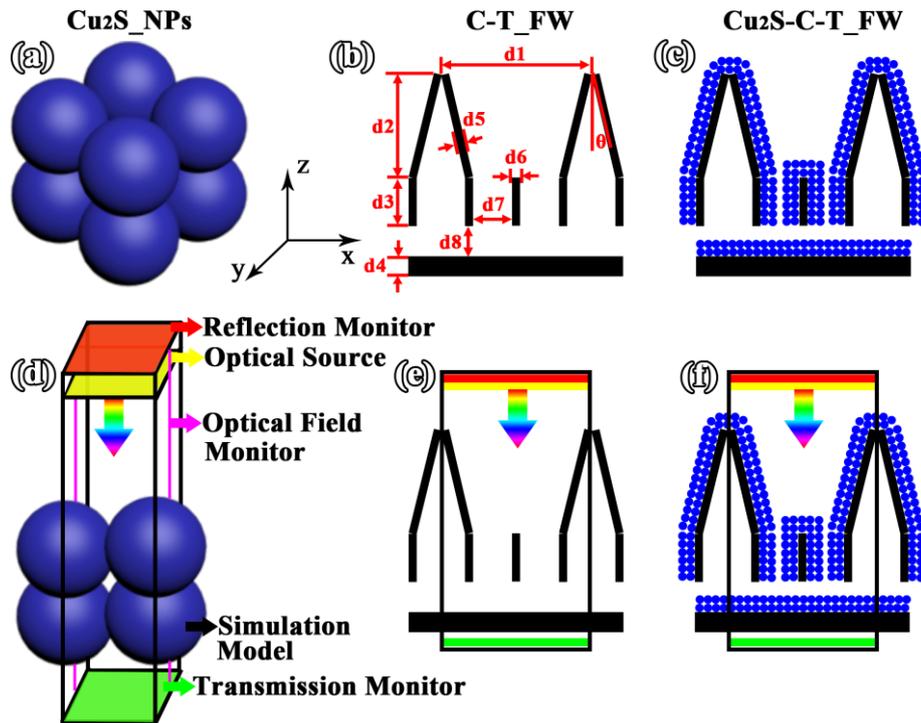
Figure S8. Schematic diagrams of (a) Cu$_2$S-NPs, (b) C-T_FW and (c) Cu$_2$S-C-T_FW, respectively. Schematic illustrations of the FDTD simulation of (d) Cu$_2$S-NPs, (e) C-T_FW and (f) Cu$_2$S-C-T_FW, respectively. Related to Figure 3.

14
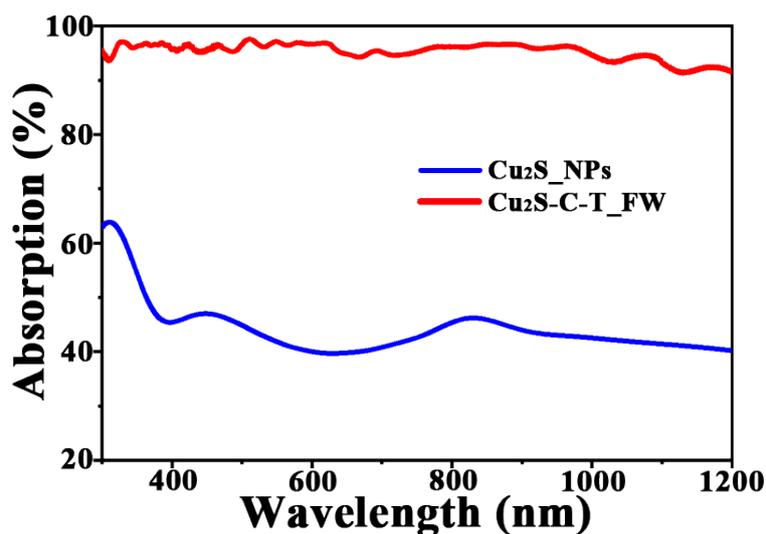
Figure S9. The FDTD simulated absorption spectra of Cu_2S-NPs and Cu_2S-C-T_FW over the wavelength range from 300 nm to 1200 nm. Related to Figure 3.
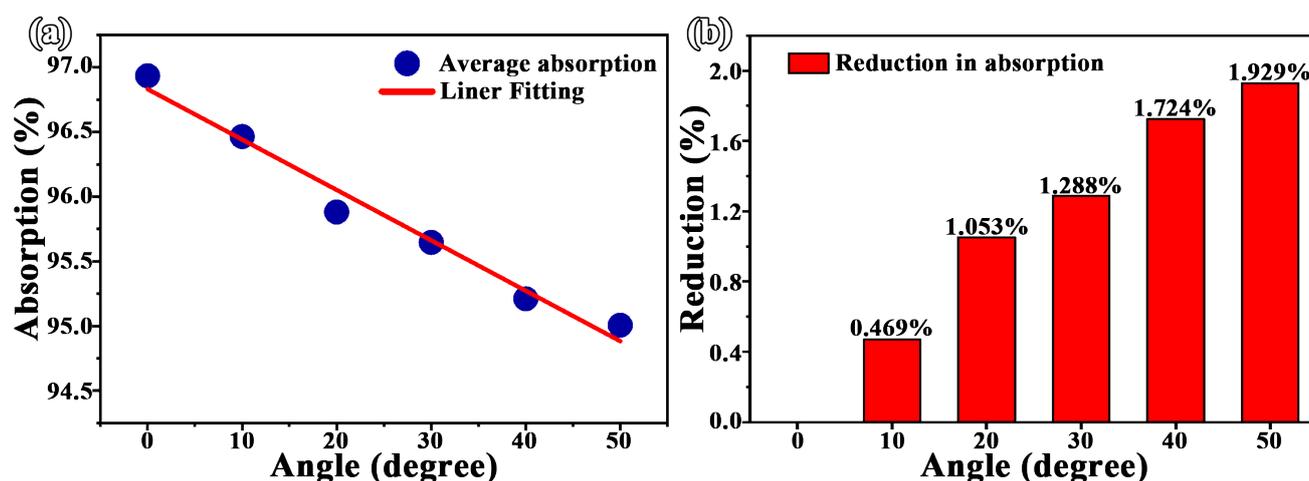
Figure S10. (a) The average absorption of Au-$Cu_{1.97}$S/Cu_2S-C-T_FW and the linear fitting of the average absorption at different incident angles. (b) The reduction of the absorption of Au-$Cu_{1.97}$S/Cu_2S-C-T_FW at different incident angles. Related to Figure 3.

Importantly, the average absorption is still greater than the 95.01% maintained at the measured wavelengths when the incident angle increases to 50° (Figure S10a). Compared with the average absorptance at the vertical incidence (0°), the reduction rate of the average absorption at the incident angles of up to 50° is only 1.929% (Figure S10b).
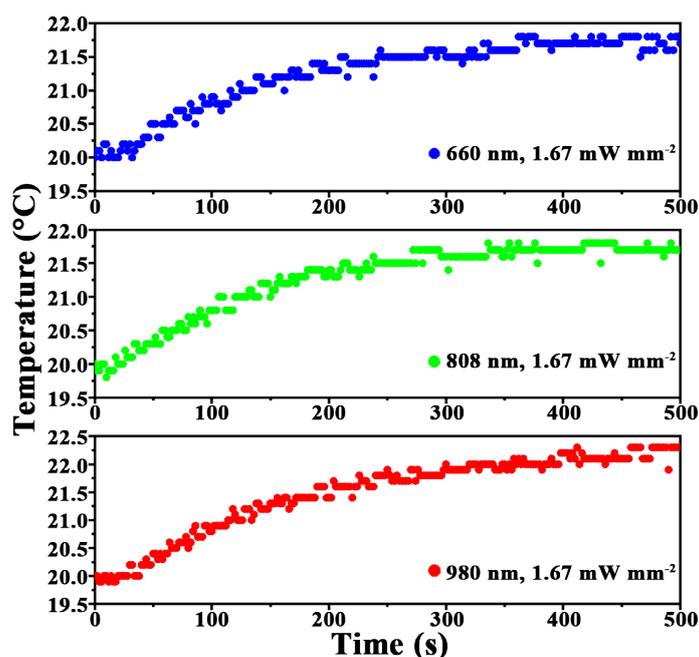
Figure S11. The temperature change of the sample of Au-Cu$_{1.97}$S/Cu$_2$S-C-T_FW during the photodetection test process. These tests are carried out at room temperature (20 °C). The incident light intensity is 1.67 mW mm^{-2}. Related to Figure 4.

Table S3. Parameters of Au-Cu$_{1.97}$S/Cu$_2$S-C-T_FW photodetector. Related to Figure 4.

Wavelength (nm)	I_{on} (μA)	I_{off} (μA)	P (mA mm^{-2})	S (mm^2)	R (mA W^{-1})	D* (Jones)	τ_{rising} (s)	τ_{decay} (s)
660	22.22	7.76	1.67	0.5	17.36	7.79×10^7	1.71	1.04
808	28.91	6.95	1.67	0.5	26.37	1.25×10^8	1.37	0.60
980	16.14	4.98	1.67	0.5	13.40	7.71×10^7	1.42	0.93
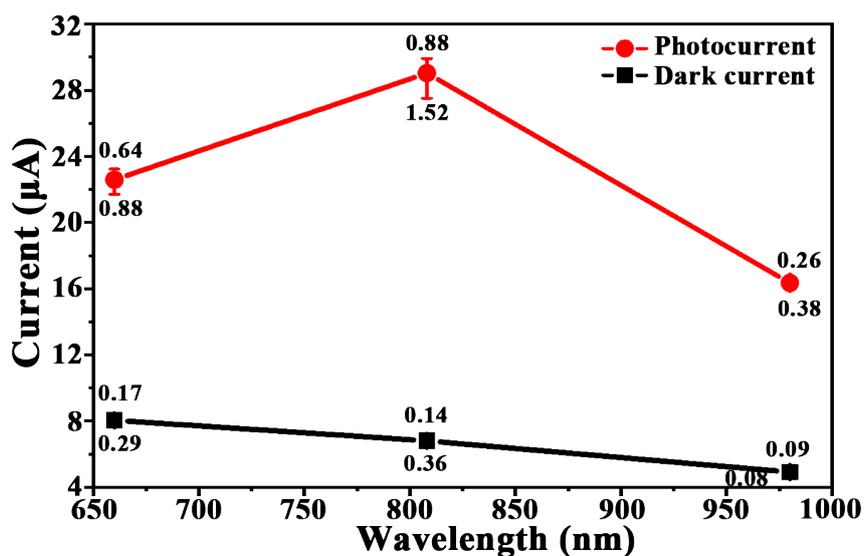
Figure S12. The error analysis of the photoresponse cycle stabilities at the light intensity of 1.67 mW mm^{-2} under incident wavelengths of 660 nm, 808 nm and 980nm, respectively. Related to Figure 4.
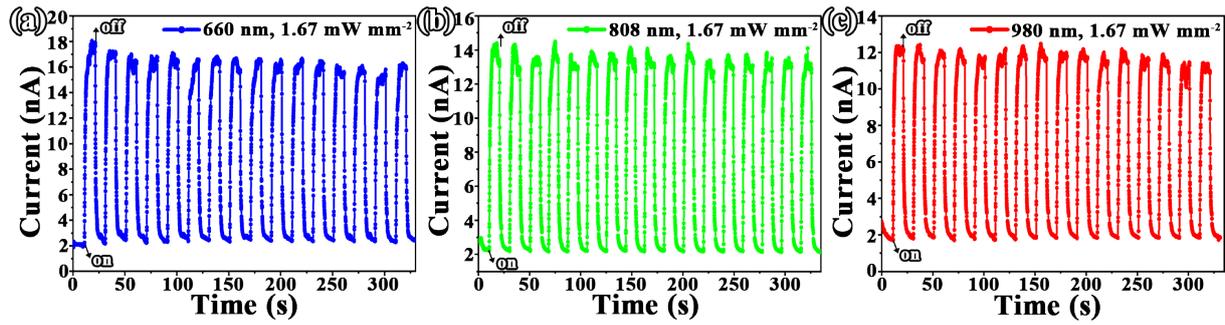
Figure S13. The photoresponse cycle stabilities of $Cu_{1.97}S/Cu_2S$-C-T_FW photodetector under different incident light (660 nm, 808nm and 980nm), respectively. Related to Figure 4.
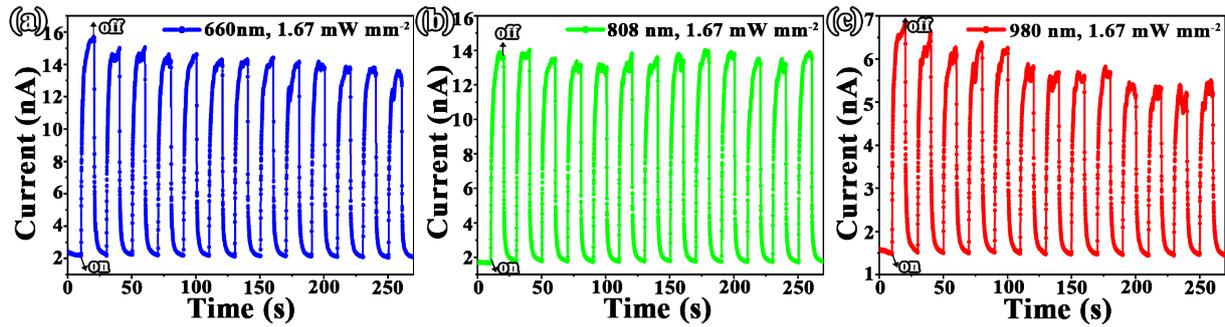
Figure S14. The photoresponse cycle stabilities of Au-$Cu_{1.97}S/Cu_2S$-C-T_FW(20 h) photodetector under different incident light (660 nm, 808nm and 980nm), respectively. Related to Figure 4.

Table S4. Parameters of $Cu_{1.97}S/Cu_2S$-C-T_FW photodetector. Related to Figure 4.

Wavelength (nm)	I_{off} (nA)	I_{on} (nA)	P (mW mm^{-2})	S (mm^{-2})	R (nA W^{-1})	D (Jones)
660	2.48	16.44	1.67	0.5	16.77	4.21×10^6
808	2.27	13.69	1.67	0.5	13.71	5.09×10^6
980	1.85	12.47	1.67	0.5	12.75	3.71×10^6

Table S5: Parameters of Au-$Cu_{1.97}S/Cu_2S$-C-T_FW(20h) photodetector. Related to Figure 4.

Wavelength (nm)	I_{off} (nA)	I_{on} (nA)	P (mW mm^{-2})	S (mm^{-2})	R (nA W^{-1})	D (Jones)
660	2.16	14.40	1.67	0.5	14.69	3.95×10^6
808	1.78	13.51	1.67	0.5	14.09	4.18×10^6
980	1.52	6.24	1.67	0.5	5.67	1.82×10^6
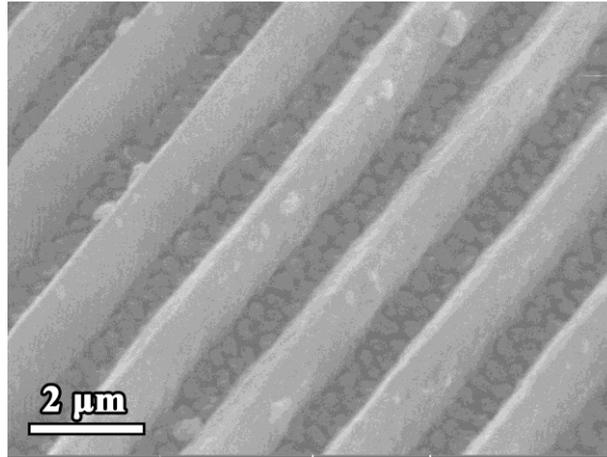
Figure S15. SEM image of Au-Cu$_{1.97}$S/Cu$_2$S-C-T_FW(20 h). Related to Figure 2.
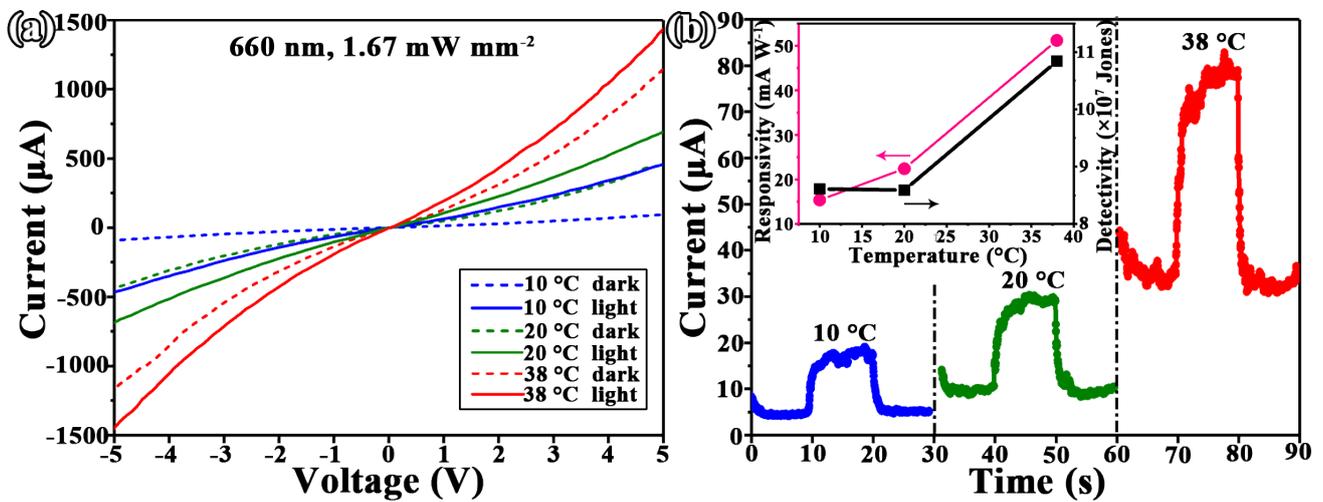
Figure S16. (a) I-V characteristics and (b) photocurrent response of Au-Cu$_{1.97}$S/Cu$_2$S-C-T_FW photodetector under optical irradiation (λ=660 nm) with an incident laser power of 1.67 mW/mm^2 under a series of testing temperatures (10 ℃, 20 ℃ and 38 ℃ and 50 ℃), at 0.1 V bias voltages, respectively. Related to Figure 6.

REFERENCES

Tan, Y., Gu, J., Zang, X., Xu, W., Shi, K., Xu, L., and Zhang, D. (2011). Versatile fabrication of intact three-dimensional metallic butterfly wing scales with hierarchical sub-micrometer structures. Angew. Chem. Int. Ed. *123*, 8457-8461.

Wu, L., Wang, W., Zhang, W., Su, H., Liu, Q., Gu, J., Deng, T., and Zhang, D. (2018). Highly sensitive, reproducible and uniform SERS substrates with a high density of three-dimensionally distributed hotspots: gyroid-structured Au periodic metallic materials. Npg Asia Materials *10*, e462-e462.

Tian, J., Zhang, W., Gu, J., Deng, T., and Zhang, D. (2015a). Bioinspired Au-CuS coupled photothermal materials: enhanced infrared absorption and photothermal conversion from butterfly wings. Nano Energy *17*, 52-62.

Smith, F.W. (1984). Optical constants of a hydrogenated amorphous carbon film. J. Appl. Phys. *55*, 764-771.

Gao, X., and Jiang, L. (2004). Biophysics: water-repellent legs of water striders. Nature *432*, 36-36.

Hao, E., and Schatz, G.C. (2004). Electromagnetic fields around silver nanoparticles and dimers. J. Chem. Phys. *120*, 357-366.

Baffou, G., Quidant, R., and Girard, C. (2010). Thermoplasmonics modeling: A Green's function approach. Phys. Rev. B

82, 165424.

Hafner, J. (2008). Ab-initio simulations of materials using VASP: Density-functional theory and beyond. J. Comput. Chem. *29*, 2044-2078.

Atwater, H.A., and Polman, A. (2010). Plasmonics for improved photovoltaic devices. Nat. Mater. *9*, 205.

Itoh, T., Yamamoto, Y.S., and Ozaki, Y. (2017). Plasmon-enhanced spectroscopy of absorption and spontaneous emissions explained using cavity quantum optics. Chem. Soc. Rev. *46*, 3904-3921.

Dion, M., Rydberg, H., Schroder, E., Langreth, D.C., and Lundqvist, B.I. (2004). Van der Waals density functional for general geometries. Phys. Rev. Lett. *92*, 246401.

Xu, Q., Huang, B., Zhao, Y., Yan, Y., Noufi, R., and Wei, S.-H. (2012). Crystal and electronic structures of Cu_xS solar cell absorbers. Appl. Phys. Lett. *100*.

Tian, J., Zhang, W., Fang, X., Liu, Q., Gu, J., Deng, T., Wang, Y., and Zhang, D. (2015b). Coupling of plasmon and 3D antireflection quasi-photonic crystal structure for enhancement infrared absorption. J. Mater. Chem. C *3*, 1672-1679.

Zhao, Q., Guo, X., Fan, T., Ding, J., Zhang, D., and Guo, Q. (2011). Art of blackness in butterfly wings as natural solar collector. Soft Matter *7*, 11433-11439.

Wang, W., Zhang, W., Fang, X., Huang, Y., Liu, Q., Bai, M., and Zhang, D. (2014). Omnidirectional light absorption of disordered nano-hole structure inspired from Papilio ulysses. Optics Lett. *39*, 4208-4211.

Arpin, K.A., Losego, M.D., Cloud, A.N., Ning, H., Mallek, J., Sergeant, N.P., Zhu, L., Yu, Z., Kalanyan, B., Parsons, G.N.*, et al.* (2013). Three-dimensional self-assembled photonic crystals with high temperature stability for thermal emission modification. Nature Commun. *4*, 2630.

Berthier, S. (2005). Thermoregulation and spectral selectivity of the tropical butterfly Prepona meander: a remarkable example of temperature auto-regulation. Appl. Phys. A *80*, 1397-1400.

Herman, A., Vandenbem, C., Deparis, O., Simonis, P., and Vigneron, J.P. (2011). Nanoarchitecture in the black wings of Troides magellanus: a natural case of absorption enhancement in photonic materials. SPIE NanoScience Engineering (International Society for Optics and Photonics) 80940H-80912.

Ding, X., Liow, C.H., Zhang, M., Huang, R., Li, C., Shen, H., Liu, M., Zou, Y., Gao, N., Zhang, Z.*, et al.* (2014). Surface plasmon resonance enhanced light absorption and photothermal therapy in the second near-infrared window. J. Am. Chem. Soc. *136*, 15684-15693.